Thomas Häffner

SIMULATION OF DYNAMICS OF QUANTUM SYSTEMS WITH CLASSICAL OPTICS

Dissertação submetida ao Programa de Pós-graduação em Fisica para a obtenção do Grau de Mestrado.
Orientador: Prof. Dr. Paulo Henrique Souto Ribeiro

Florianópolis

2018

Ficha de identificação da obra elaborada pelo autor,
através do Programa de Geração Automática da Biblioteca Universitária da UFSC.

Häffner, Thomas
Simulation of dynamics of quantum systems with classical optics / Thomas Häffner ; orientador, Paulo Henrique Souto Ribeiro, 2018.
90 p.

Dissertação (mestrado) - Universidade Federal de Santa Catarina, Centro de Ciências Físicas e Matemáticas, Programa de Pós-Graduação em Física, Florianópolis, 2018.

Inclui referências.

1. Física. 2. Ótica, Termodinâmica, simulação quântica. I. Souto Ribeiro, Paulo Henrique. II. Universidade Federal de Santa Catarina. Programa de Pós-Graduação em Física. III. Título.

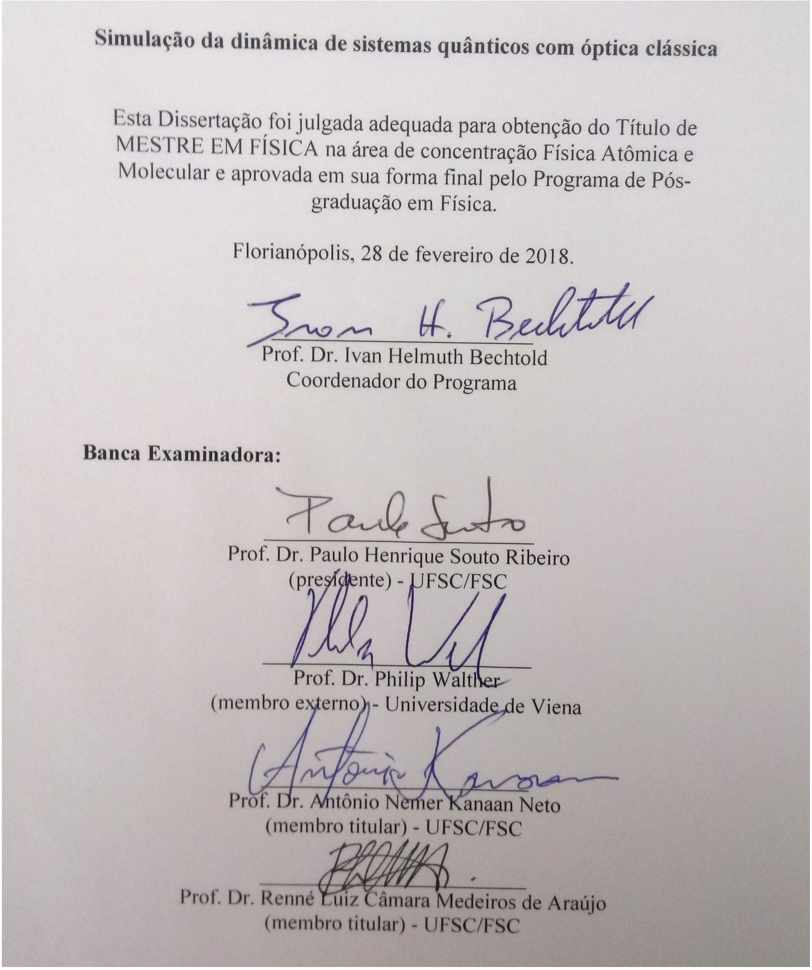

Simulação da dinâmica de sistemas quânticos com óptica clássica

Esta Dissertação foi julgada adequada para obtenção do Título de MESTRE EM FÍSICA na área de concentração Física Atômica e Molecular e aprovada em sua forma final pelo Programa de Pós-graduação em Física.

Florianópolis, 28 de fevereiro de 2018.

Ivan H. Bechtold

Prof. Dr. Ivan Helmuth Bechtold
Coordenador do Programa

Banca Examinadora:

Paulo Souto

Prof. Dr. Paulo Henrique Souto Ribeiro
(presidente) - UFSC/FSC

Prof. Dr. Philip Walther
(membro externo) - Universidade de Viena

Antônio Kanaan

Prof. Dr. Antônio Nemer Kanaan Neto
(membro titular) - UFSC/FSC

Prof. Dr. Renné Luiz Câmara Medeiros de Araújo
(membro titular) - UFSC/FSC

AGRADECIMENTOS

I would first like to thank my advisor Prof. Dr. Paulo Henrique Souto Ribeiro. The door to his office was always open whenever I needed help or advice and whenever I had a question about my research or writing.

In the same way I want to thank Prof. Dr. Renné Medeiros de Araújo. He helped me as a co-worker, teacher and even though not listed as such in this work as a co-advisor.

I would like to thank everyone that helped me in the process of developing material in this work such as illustrations or plots: Renné Medeiros de Araújo, Willamys Cristiano Soares Silva and Maria Fernanda Ramos Lento.

I would also like to thank the experts who were involved in the validation survey for this research project: R. Bernardi , D. S. Tasca, M. P. J. Lavery, M. J. Padgett, A. Kanaan, L. C. Céleri.

Finally I want to express my very profound gratitude to my parents and to my spouse and my parents-in-law for unfailing support and encouragement throughout my years of study and through the process of researching and writing this thesis. This accomplishment would not have been possible without them. Thank you.

RESUMO

A área de estudo da termodinâmica fora do equilíbrio e teoria da informação quântica são atualmente objeto de crescente interesse teórico e experimental. Nesse trabalho, nós apresentamos uma plataforma experimental para estudar aspectos termodinâmicos de sistemas quânticos multi-dimensionais. Nós usamos os feixes Laguerre-Gaussianos, mais especificamente o momento angular orbital desses modos ópticos, junto com a analogia entre a equação da onda paraxial e a equação do Schrödinger, para emular os autoestados da energia de um oscilador harmônico quântico. Nós simulamos evoluções quânticas e aplicamos processos a esses feixes de luz com um modulador espacial de luz. A distribuição de probabilidade do trabalho associado a esses processos é reconstruída experimentalmente empregando o chamado ”esquema de duas medidas” (em inglês: ”two point measurement scheme”) para definir trabalho num sistema quântico. A relação da flutuação de Jarzynski é avaliada e verificada. Nós também abordamos o paradigma do ”Demônio de Maxwell” que explora o papel da informação como recurso num processo físico. Nós propomos uma montagem experimental para realizar o demônio de Maxwell com a plataforma apresentada neste trabalho, ilustrando a sua utilidade. Em uma primeira abordagem, nós utilizamos dados experimentais pós-selecionados, que emulam a ação do demônio, para avaliar o efeito de sua ação no sistema. Em seguida, nós utilizamos uma segunda metodologia experimental para implementar o mecanismo de medida e realimentação relativos à ação do demônio de Maxwell. Os resultados foram empregados mais uma vez para avaliar a relação de Jarzynski com a presença do mecanismo do demônio de Maxwell.

Palavras-chave: Modos de Laguerre-Gauss. Momento angular orbital da luz. Teorema de flutuação de Jarzynski. Demônio de Maxwell.

RESUMO EXPANDIDO

Introdução

A termodinâmica fora do equilíbrio e a teoria da informação quântica são campos de pesquisa inter-relacionados e atualmente objetos de crescente interesse teórico e experimental. Em 1992 Allen *et al.* descobriu que feixes de luz com frentes de fase helicoidais carregam um momento angular orbital, que é distinto e adicional ao momento angular orbital de spin (ALLEN et al., 1992). A família natural de modos óticos que contém um momento angular orbital são os modos Laguerre-Gaussianos que são descritos pelo seu número radial p e o número azimutal ℓ. Com isso, os fótons nesses estados são qudits fotônicos, já que mais de um bit de informação pode ser codificado em cada fóton. Esta propriedade pode ser usada para simular um sistema quântico. Aqui empregaremos esses modos ópticos para propor uma nova plataforma para estudar propriedades fora do equilíbrio de sistemas quânticos multi-dimensionais usando apenas luz clássica.

Objetivos

Modos Laguerre-Gaussianos são soluções para a equação da onda paraxial e são descritos por números quânticos discretos. Por causa da analogia entre a equação paraxial e a equação Schrödinger, os perfis de amplitude transversal dos modos Laguerre-Gaussianos são formalmente idênticos aos auto-estados de energia do oscilador harmônico quântico bidimensional. Esta propriedade faz dos feixes Laguerre-Gaussianos um candidato ideal para simular sistemas quânticos multi-dimensionais e as evoluções deles. Usamos os feixes Laguerre-Gaussianos, mais especificamente o momento angular orbital desses modos ópticos, para estudar experimentalmente alguns aspectos termodinâmicos de um sistema quântico de alta dimensionalidade. Estudamos aspectos da termodinâmica fora de equilíbrio do sistema simulado, avaliando o teorema de flutuação de Jarzynski com base em dados medidos. Sugerimos uma configuração experimental que implemente um demônio de Maxwell usando a plataforma apresentada aqui para demonstrar a utilidade de tal demônio. Em um segundo experimento, um demônio de Maxwell será implementado no sistema e o teorema de flutuação de Jarzynski será avaliado novamente. Nós fornecemos uma nova plataforma experimental para implementar essas simulações de sistemas quânticos de alta dimensionalidade e suas evoluções usando apenas luz clássica.

Metodologia

Todos os experimentos foram realizados no laboratório de ótica quântica e no laboratório de astrofísica do Instituto de Física da UFSC. Um laser de HeNe e, num segundo experimento, um laser de diodo foram usados como fontes de luz. Os moduladores espaciais de luz (SLM) criam modos Laguerre-Gaussianos após reflexão, modulando as fases relativas da frente de onda. Da mesma forma, o momento angular orbital de um feixe de luz pode ser manipulado. Isso nos permite usar SLMs para simular sistemas quânticos e suas evoluções. A ação desses SLMs foi programada e calculada em um computador usando *LabVIEW*. Depois que o sistema passou por uma evolução ou processo, medimos o estado final do sistema com um dispositivo chamado classificador de modo e uma câmera CCD. A distribuição de probabilidade de trabalho desses processos é reconstruída experimentalmente empregando o chamado ”esquema de duas medidas”(em inglês: ”two-point measurement scheme”) para definir trabalho num sistema quântico. A relação de flutuação de Jarzynski é avaliada e verificada. Em seguida, incluímos o demônio de Maxwell, que explora o papel da informação como um recurso em um processo físico. Em uma primeira abordagem, nós utilizamos dados experimentais pós-selecionados, que emulam a ação do demônio, para avaliar o efeito de sua ação no sistema. Além disso, usamos uma segunda metodologia experimental para implementar um mecanismo de medida e realimentação relativos à ação do demônio de Maxwell. Nesse experimento, a informação da geração do sistema inicial pode ser extraída e usada para diminuir a entropia do sistema. Os resultados foram utilizados novamente para avaliar a relação de Jarzynski na presença de um demônio de Maxwell. Para processar os dados registrados, um ajuste linear aos dados de calibração foi feito, usando programas de computador escritos nas linguagens *Mathematica, Python* e *R.*

Resultados e Discussão

Nos experimentos, os processos aplicados mudam os níveis simulados da energia do sistema. As probabilidades condicionais de transição foram calculando medindo o momento angular orbital na saída e foram então usadas para calcular a distribuição de probabilidade do trabalho. O teorema de Jarzynski pode ser avaliado para esse processo. Considerando o aumento da entropia devido à medição do mundo real, as flutuações do ruído térmico do laser e da câmera, bem como a imperfeição experimental, encontramos uma boa concordância com os resultados previstos teoricamente. Estes resultados foram publicados em um jornal científico. Da mesma maneira que antes, nós avaliamos a desigualdade de Jarzynski para um processo que inclui a ação de um demônio de

Maxwell e mostramos que um demônio estava agindo de fato e que os dados medidos estão de acordo com a previsão teórica. Estes resultados mostram a utilidade dos modos Laguerre-Gauss e, portanto, do momento angular orbital para simular sistemas quânticos, aqui um oscilador quântico harmônico bidimensional. A plataforma experimental apresentada neste trabalho permite o estudo da termodinâmica fora do equilíbrio, pois permite medidas projetivas dos níveis da energia do sistema.

Considerações Finais
Em conclusão, nós investigamos experimentalmente a versão quântica do trabalho termodinâmico e a relação de flutuação de Jarzynski usando o momento angular orbital da luz, um grau discreto de liberdade com dimensão infinita usualmente empregado no regime de fótons único para realizar um qudit, com aplicações em comunicação quântica e processamento de informação quântica. Nossos resultados ilustram a utilidade dos feixes Laguerre-Gaussianos como uma plataforma prática para investigar aspectos do campo crescente da termodinâmica quântica em espaços de Hilbert da alta dimensão. Dada a versatilidade desta plataforma, pode-se considerar a sua utilização, por exemplo, no estudo do papel do emaranhamento multipartido nos processos termodinâmicos, bem como o papel do ambiente, isto é, processos não-unitários e não-unital.

Palavras-chave: Modos de Laguerre-Gauss. Momento angular orbital da luz. Teorema de flutuação de Jarzynski. Demônio de Maxwell.

ABSTRACT

The field of non-equilibrium thermodynamics and quantum information theory have shown an increased theoretical and experimental interest. In this work we provide an experimental platform for studying thermodynamical aspects of high dimensional quantum systems. We use Laguerre-Gaussian beams, more specifically the orbital angular momentum of those optical modes and make use of the analogy between the paraxial wave equation and the Schrödinger equation to emulate the energy eigenstates of a quantum harmonical oscillator. We simulate quantum evolutions and apply processes to those light beams by the use of a spatial light modulator. The work probability distribution of those processes is experimentally reconstructed by employing the two-point measurement scheme to define work in a quantum system. The Jarzynski's fluctuation relation is evaluated and verified. Maxwell's demon explores the role of information as a resource in a physical process. We suggest a experimental setup that implements a Maxwell's demon using the platform presented here to demonstrate its usefulness. In a first approach we employ post-selected experimental data, which emulates the action of a demon, in order to evaluate the effect of that action onto the system. Furthermore, we used a second experimental methodology in order to implement a measurement feedback control mechanism concerning the action of the Maxwell's demon. The results were used again to evaluate the Jarzynski's relation in the presence of a Maxwell's demon.

Keywords: Laguerre-Gaussian modes. Orbital angular momentum of light. Jarzynski's fluctuation theorem. Maxwell's demon.

LISTA DE FIGURAS

Figura 1 When a light beam has a ℓ helical interwinded phasefronts, each photon carries an orbital angular momentum of $\ell\hbar$. Image taken from (COMMONS, 2011). 19

Figura 2 Lateral view of a Gaussian beam propagating along z. . 27

Figura 3 Typical normalized intensity profiles for some Hermite-Gaussian modes. 28

Figura 4 Normalized intensity profiles of Laguerre-Gaussian modes. 29

Figura 5 a) Arrangement for producing a hologram; b) use of the hologram in producing the real and virtual images. 31

Figura 6 Simulation of an interference pattern of a Laguerre-Gaussian beam ($\ell = 3,\ p = 0$) and a plane wave. 32

Figura 7 Schematic illustration of the forward trajectory (green) and its conjugate reversed trajectory (orange), with the relation of reversed momenta and time between them according to equation (3.28). 42

Figura 8 Illustration of the action of a Maxwell's demon. After the system initially in state ρ_0 is driven unitarily ($\mathcal{U}$), the demon uses the outcome l of the measurement $\mathcal{M}_l$ to apply a controlled evolution $\mathcal{F}^k$. 46

Figura 9 Experimental setup: SLM1 creates input OAM modes from the expanded laser beam. SLM2 applies an action to the beam which is then analysed by a mode sorter. 49

Figura 10 Images recorded with a CCD camera after Laguerre-Gaussian beams passed through a mode sorter. The image in a) was recorded for a beam for $\ell = -7$ and the image in b) for a superposition of $\ell = -12$ and $\ell = -2$. 50

Figura 11 Intensity distributions after the mode sorter when the process $(\mathcal{L}_{+5} + \mathcal{L}_{-5})/\sqrt{2}$ is applied to the input modes (a) $\ell = -7$ and (b) $\ell = 3$. In gray are the calibration curves for the input modes ranging from $\ell = -15$ to $\ell = +15$ without any process applied by SLM2. 51

Figura 12 Normalized intensity distribution as a function of $|\ell|$ for $\beta\hbar\omega = 0.67 \pm 0.01$. 52

Figura 13 Image of the SLM model PLUTO-2 by HOLOEYE. 53

Figura 14 Example for $\ell = 3$. Combination of the phase distribution and a phase ramp resulting in a forked diffraction grating. . . . 54

Figura 15 Illustration of the *mode sorter* scheme with the intensity of the beam in different planes along the axis of propagation for a LG mode ($\ell = 1$). Illustration taken from Ref. (ALMEIDA, 2015) . . 55

Figura 16 Sketch of the general process of determining the OAM of a LG beam using a mode sorter. The OAM components get separated along the x-axis and recorded by a CCD camera. The image is integrated along the y-axis. 56

Figura 17 Conditional probabilities for the process $(\mathcal{L}_{+5}+\mathcal{L}_{-5})/\sqrt{2}$. Input and output are vertical and horizontal axis, respectively. (a) Transition matrix obtained from the recorded experimental data for input modes $-7 \leq \ell \leq 7$. (b) Theoretical prediction for the same process. 59

Figura 18 Experimentally reconstructed work probability distribution for $\beta\hbar\omega = 2$ for the process $(\mathcal{L}_{+5} + \mathcal{L}_{-5})/\sqrt{2}$. 61

Figura 19 Plot of the fluctuation relation $\langle e^{-\beta W}\rangle$ for the process $(\mathcal{L}_{+5} + \mathcal{L}_{-5})/\sqrt{2}$. The curve labeled *exp* was obtained from experimental data and the curve labeled *theory* is the theoretically calculated curve for the same process. 62

Figura 20 Experimental setup for a protocol including a Maxwell's demon. After SLM1 generates LG modes from an initial Gaussian laser beam, mode sorter MS1 separarates the modes according to the sign of their OAM (ℓ). Mode sorters MS2, MS3 and MS4 are working in reverse, transforming the light beams into OAM modes, which get spatially modulated by SLM2, SLM3 and SLM4. The OAM of the resulting beams is measured by a mode sorter and a CCD camera (MS5+CCD1, MS6+CCD2 and MS7+CCD3). 63

Figura 21 Conditional probabilities for the process $(\mathcal{L}_{+5}+\mathcal{L}_{-5})/\sqrt{2}$ including the action of a Maxwell's demon. Input and output are vertical and horizontal axis, respectively. (a) Transition matrix obtained from the post-selected recorded experimental data for input modes $-7 \leq \ell \leq 7$. (b) Theoretical prediction for the same process. 65

Figura 22 Experimentally reconstructed work probability distribution for $\beta\hbar\omega = 2$ for the process $(\mathcal{L}_{+5} + \mathcal{L}_{-5})/\sqrt{2}$, including the action of a Maxwell's Demon. 66

Figura 23 Plot of the fluctuation relation $\langle e^{-\beta W}\rangle$ for the process $(\mathcal{L}_{+5} + \mathcal{L}_{-5})/\sqrt{2}$ including the action of a Maxwell's demon. The curve labeled *exp* was obtained from experimental data and the curve labeled *theory* is the theoretically calculated curve for the same process. 67

Figura 24 Plot of the fluctuation relation $\langle e^{-\beta W} \rangle$ for the process $(\mathcal{L}_{+1} + \mathcal{L}_{-1} + \mathcal{L}_0)/\sqrt{3}$. The curve labeled *exp* was calculated from experimental data, the curve labeled *exp/ideal* was calculated for the random input states, but for a theoretically computed ideal process and the curve labeled *theory* was calculated for a theoretical thermal state for an ideal process. 70

Figura 25 Plot of the fluctuation relation $\langle e^{-\beta W} \rangle$ for the process $(\mathcal{L}_{+1} + \mathcal{L}_{-1} + \mathcal{L}_0)/\sqrt{3}$. The plot in a) is showing the relation between $\langle e^{-\beta W} \rangle$ and $\beta\hbar\omega$ for different fixed values of $\mathcal{I}$, and plot b) is showing the relation between $\langle e^{-\beta W} \rangle$ and $\mathcal{I}$ for different fixed values of $\beta\hbar\omega$. 71

Figura 26 Beam path to use one SLM for two separate spatial modulations by dividing the screen into half. 89

SUMÁRIO

1 INTRODUCTION 19

2 THE PARAXIAL WAVE EQUATION AND GAUSSIAN BEAMS 23

2.1 THE PARAXIAL WAVE EQUATION 23

2.1.1 Derivation 23

SOLUTIONS 26

2.1.2 Gaussian Beams 26

2.1.3 Hermite-Gaussian Beams 27

2.1.4 Laguerre-Gaussian beams 28

2.2 PRODUCTION OF LAGUERRE-GAUSSIAN BEAMS . . 29

2.2.1 Holograms 29

3 QUANTUM THERMODYNAMICS AND SIMULATION WITH CLASSICAL LIGHT 33

3.1 SIMULATION OF A QUANTUM HARMONIC OSCILLATOR WITH CLASSICAL LIGHT 33

3.2 SIMULATION SCHEME 34

3.2.1 Qantum harmonic oscillator formalism 34

3.3 THERMAL STATES 36

3.3.1 Simulation of thermal states 38

3.4 WORK DISTRIBUTION 39

3.5 JARZYNSKI THEOREM 40

ENTROPY PRODUCTION 44

3.6 MUTUAL INFORMATION AND MAXWELL‘S DEMON 45

4 EXPERIMENT 49

4.1 EXPERIMENTAL SETUP 49

4.2 SPATIAL LIGHT MODULATOR 53

4.3 MODE SORTER 54

4.4 DETERMINATION OF THE ORBITAL ANGULAR MOMENTUM 55

5 RESULTS 59

5.1 SIMULATION OF A QUANTUM SYSTEM 59

5.2 MAXWELL’S DEMON 61

5.2.1 Experimental scheme for a Maxwell’s Demon 62

5.2.2 Post-selected Process 64

5.2.3 Experimental implementation of a Maxwell’s Demon 67

6 CONCLUSIONS 73

REFERÊNCIAS 75
APÊNDICE A – Measurement uncertainty 85
APÊNDICE B – Differences in experimental setup 89

1 INTRODUCTION

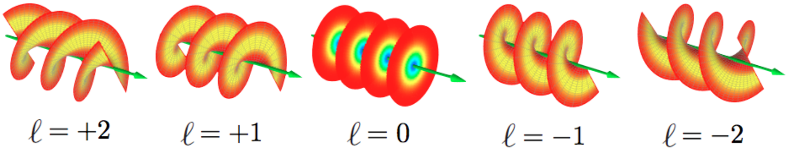

Figura 1 – When a light beam has a ℓ helical interwinded phasefronts, each photon carries an orbital angular momentum of $\ell\hbar$. Image taken from (COMMONS, 2011).

It was first suggested by Poynting in 1909 that circularly polarized light carries an angular momentum (POYNTING, 1909), which later led to the discovery that circularly polaized photons carry a spin angular momentum (SAM) of $\pm\hbar$ per photon. It took almost another century until Allen *et al.* found out in 1992 that a light beam possessing helical phase fronts carries an orbital angular momentum (OAM), which is distinct from, and additional to the SAM (ALLEN et al., 1992). If a light beam has ℓ interwinded helical phase fronts, then each photon carries an average OAM of $\ell\hbar$ (Fig. 1). The natural family of optical modes containing orbital angular momentum are the Laguerre-Gaussian (LG) modes. Those modes are solutions to the paraxial wave equation and are characterized by their radial number p and their azimuthal number ℓ (SALEH; TEICH, 2001). The study and application of these modes are fairly recent and are increasing with time (ALLEN et al., 1992; PADGETT; ALLEN, 2000; PADGETT, 2014). Because the indices p and ℓ are discrete numbers, photons populating LG modes with OAM are a realization of high-dimensional quantum states (VAZIRI; WEIHS; ZEILINGER, 2002; DADA et al., 2011; GIOVANNINI et al., 2013; KRENN et al., 2014), making them photonic qudits, as more than one bit of information can be encoded in each photon. Therefore their utilization has been explored in quantum communication schemes and quantum information processing (MOLINA-TERRIZA; TORRES; TORNER, 2001; BOURENNANE; KARLSSON; BJÖRK, 2001; HUBER; PAWŁOWSKI, 2013).

Furthermore, the transverse amplitude profiles of LG modes are formally equivalent to the energy eigenstates of the two-dimensional quantum harmonic oscillator. This property and the analogy between the paraxial equation and the Schrödinger equation makes Laguerre-

Gaussian modes an ideal candidate in order to emulate these quantum systems and their evolution (NIENHUIS; ALLEN, 1993), as they can be created and manipulated experimentally with the use of a spatial light modulator (SLM). In this work we use LG modes to study experimentally some thermodynamical aspects of a high dimensional quantum system.

Out-of-equilibrium thermodynamics studies the response of a system under external perturbation and led to important statements for the thermodynamics of small systems undergoing quantum mechanical evolutions (ESPOSITO; HARBOLA; MUKAMEL, 2009; CAMPISI; HÄNGGI; TALKNER, 2011). While the theory of the linear response (CALLEN; WELTON, 1951) was developed based on previous works like Refs. (EINSTEIN, 1926; JOHNSON, 1928), the information about the complete nonlinear response, on the other hand, is captured by the fluctuation theorems. These relations connect the equilibrium properties of a thermodynamical system with the non-equilibrium features. Considering that new technologies try to minimize the size of devices (HÄNGGI; MARCHESONI, 2009), these fluctuations and time scales have gained more importance and more attention in recent theoretical and experimental studies (RITORT, 2007; ESPOSITO; HARBOLA; MUKAMEL, 2009; CAMPISI; HÄNGGI; TALKNER, 2011). Fluctuation theorems such as the Crook's theorem (CROOKS, 1998) and the Jarzynski's theorem (JARZYNSKI, 1997) have been developed based on publications by Bochkov and Kuzovlev (Bochkov; Kuzovlev, 1977; BOCHKOV; KUZOVLEV, 1981). These theorems have been proven for classical (Bochkov; Kuzovlev, 1977; JARZYNSKI, 1997; CROOKS, 1998), as well as for quantum systems (Tasaki, 2000; CAMPISI; TALKNER; HÄNGGI, 2011). The quantum versions of those relations are only possible due to the two-point measurement approach to define work. In this approach, work is defined as the difference between two energy projective measurements on the system. One before and one after a considered process takes place.

The experimental study of such fluctuation relations is new, especially in quantum systems, as performing energy projective measurements is a difficult obstacle to overcome. To our knowledge, so far, the only experiment using this approach was reported in Ref. (AO et al., 2014), where trapped ions were used to investigate the work statistics associated with a harmonic oscillator.

With the present work we contribute to this line of research by providing a new experimental platform for the investigation of thermodynamic processes in the quantum regime.

We make use of an optical setup with Laguerre-Gaussian beams that simulates a two dimensional quantum harmonic oscillator. By spatially modulating the light beams, we apply a given process and are able to reconstruct the work probability distribution of that process by employing the projective measurement scheme. These results have been published in a scientific journal (ARAúJO et al., 2018). Moreover, we experimentally implement a Maxwell's demon acting on this system. In the Maxwell's demon paradigm, information about the microscopic states of the system is used to artificially reduce the entropy. This would be a violation of the second law of thermodynamics, if we do not account for the role of information.

2 THE PARAXIAL WAVE EQUATION AND GAUSSIAN BEAMS

2.1 THE PARAXIAL WAVE EQUATION

2.1.1 Derivation

Electric fields and therefore light propagates in the form of waves. Let us consider the electromagnetic field in the vacuum. It can be described by a scalar potential or by some vectorial density distribution like the electric field, $\vec{E}$, magnetic field $\vec{H}$ or the potential vector $\vec{A}$. The Maxwell's equations (FOWLES, 1975) relate electric and magnetic fields to each other, and each one of them to their respective sources:

$$\nabla \times \boldsymbol{E} = -\mu_0 \frac{\partial \boldsymbol{H}}{\partial t} \tag{2.1}$$

$$\nabla \times \boldsymbol{H} = \epsilon_0 \frac{\partial \boldsymbol{E}}{\partial t} \tag{2.2}$$

$$\nabla \cdot \boldsymbol{E} = 0 \tag{2.3}$$

$$\nabla \cdot \boldsymbol{H} = 0 \ , \tag{2.4}$$

where μ_0 is the permeability of the vacuum and ϵ_0 is the permittivity of the vacuum. If we take the curl of equations (2.1) and (2.2) and use the fact that the order of time and space differentiation is reversible, we can separate $\boldsymbol{E}$ and $\boldsymbol{H}$ leading to:

$$\nabla \times (\nabla \times \boldsymbol{E}) = -\mu_0 \epsilon_0 \frac{\partial^2 \boldsymbol{E}}{\partial t^2} \tag{2.5}$$

$$\nabla \times (\nabla \times \boldsymbol{H}) = -\mu_0 \epsilon_0 \frac{\partial^2 \boldsymbol{H}}{\partial t^2} \ . \tag{2.6}$$

By using equations (2.3) and (2.4) and the vector identity

$$\nabla \times (\nabla \times \quad) = \nabla(\nabla \cdot \quad) - \nabla^2(\quad) \ , \tag{2.7}$$

we obtain from equations (2.5) and (2.6)

$$\nabla^2 \boldsymbol{E} = \frac{1}{c^2}\frac{\partial^2 \boldsymbol{E}}{\partial t^2} \tag{2.8}$$

$$\nabla^2 \boldsymbol{H} = \frac{1}{c^2}\frac{\partial^2 \boldsymbol{H}}{\partial t^2} \ , \tag{2.9}$$

where $c = 1/(\mu_0 \epsilon_0)$ is the speed of light. Eqs. (2.8) and (2.9) can be written in the same form for each vector component. For instance, in Cartesian coordinates, x, y and z components satisfy equations of the same form. Thus, a general scalar field satisfies the equation

$$\Delta u - \frac{1}{c^2}\frac{\partial^2 u}{\partial t^2} = 0 \quad , \tag{2.10}$$

where Δ is the Laplace operator, $\Delta = \partial^2/\partial x^2 + \partial^2/\partial y^2 + \partial^2/\partial z^2$. This equation is called the wave equation and any solution $u(\boldsymbol{r}, t)$ with position $\boldsymbol{r} = (x, y, z)$ and time t is called a wave function.

One possible solution is the monochromatic wavefunction (FOWLES, 1975)

$$u(\boldsymbol{r}, t) = a(\boldsymbol{r})e^{-i\omega t}, \tag{2.11}$$

with the complex amplitude $a(\boldsymbol{r})$ and the frequency ω. Substituting this into the wave equation (2.10) leads to the differential equation

$$(\Delta + k^2)a(\boldsymbol{r}) = 0, \tag{2.12}$$

where $k = \omega/c$ is the wave number and c the speed of light. Equation (2.12) is called the Helmholtz equation.

In the experiments of this work we use a laser as a source of light. This means that the light beam is nearly collimated and does not diverge or converge too much, so that we can apply the paraxial approximation. The wavevectors $\vec{k}$ of a paraxial wave are approximately paralell to the direction of propagation (SALEH; TEICH, 2001). We will use these properties of the light beam to find more specific solutions for the Helmholtz equation (2.12).

To describe a paraxial wave we take the spatial part of the wave [eq. (2.11)], and write it in terms of an envelope function $C(r)$ that varies slowly with the longitudinal coordinate z multiplied by a propagation phase:

$$a(\boldsymbol{r}) = C(\boldsymbol{r})e^{-ikz} \ . \tag{2.13}$$

Varying slowly along the propagation direction z means that the variation $\Delta C \ll C$ for a distance $\Delta z \approx \lambda$, that is to say

$$\Delta C = \frac{\partial C}{\partial z}\Delta z \approx \frac{\partial C}{\partial z}\lambda \ll C \ . \tag{2.14}$$

It follows that

$$\frac{\partial C}{\partial z} \ll \frac{C}{\lambda} = \frac{Ck}{2\pi} \ . \tag{2.15}$$

Taking the derivative of the inequality (2.15) with respect to z

$$\begin{aligned} \frac{\partial^2 C}{\partial z^2} &\ll \frac{k}{2\pi}\frac{\partial C}{\partial z} \\ \Leftrightarrow \frac{\partial^2 C}{\partial z^2} &\ll \frac{k^2 C}{4\pi^2}, \end{aligned} \tag{2.16}$$

we can see that the second derivative varies slowly with the square of the wave number.

Now we substitute the equation (2.13) into (2.12) and neglect $\frac{\partial^2 C}{\partial z^2}$ compared with $k\frac{\partial C}{\partial z}$ or $k^2 C$:

$$\begin{aligned} & \left(\frac{\partial^2 a}{\partial x^2} + \frac{\partial^2 a}{\partial y^2} + \frac{\partial^2 a}{\partial z^2}\right) + k^2 a = 0 \\ \Rightarrow \quad & e^{-ikz}\left(\frac{\partial^2 C}{\partial x^2} + \frac{\partial^2 C}{\partial y^2}\right) - e^{-ikz}\ 2ik\frac{\partial C}{\partial z} - e^{-ikz}\ k^2 C + e^{-ikz}\ k^2 C = 0 \\ \Rightarrow \quad & \left(\frac{\partial^2}{\partial x^2} + \frac{\partial^2}{\partial y^2} - 2ik\frac{\partial}{\partial z}\right) C = 0 \\ \Rightarrow \quad & \Delta_T C - 2ik\frac{\partial}{\partial z}C = 0, \end{aligned} \tag{2.17}$$

where $\Delta_T = \frac{\partial^2 c}{\partial x^2} + \frac{\partial^2 c}{\partial y^2}$ is the transverse Laplace operator.

Equation (2.17) is called the paraxial Helmholtz equation.

2.1.2 Gaussian Beams

One solution to the paraxial Helmholtz equation (2.17) are the Gaussian beams (SALEH; TEICH, 2001; SVELTO, 1976).

$$C = \frac{c_0}{q(z)} e^{-ik\left(\frac{x^2+y^2}{2q(z)}\right)}, \tag{2.18}$$

where c_0 is a constant, k is the wave number and $q(z)$ is defined as:

$$\frac{1}{q(z)} = \frac{1}{R(z)} - i\frac{\lambda}{\pi w(z)^2}, \tag{2.19}$$

where λ is the wavelength, $R(z)$ is the wavefront radius of curvature and $w(z)$ is the beam width. $R(z)$ can be written as

$$R(z) = z\left(1 + \left(\frac{\pi w_0^2}{\lambda z}\right)^2\right) = z\left(1 + \left(\frac{z_R}{z}\right)^2\right). \tag{2.20}$$

The beam intensity has its peak on the beam axis and decreases by a factor of $1/e^2$ at the radial distance $\rho = \sqrt{x^2+y^2} = w(z)$ (see Fig. 2) where

$$w(z) = w_0\left(1 + \left(\frac{\lambda z}{\pi w_0^2}\right)^2\right)^{1/2} = w_0\left(1 + \left(\frac{z}{z_R}\right)^2\right)^{1/2}. \tag{2.21}$$

$w(z)$ has a minimum, and the origin of z is usually defined so that $w(z=0) = w_0$, where w_0 is called beam waist. $w(z)$ increases with z and reaches $\sqrt{2}w_0$ at $z = z_R$, called the Rayleigh range (illustrated in Fig 2).

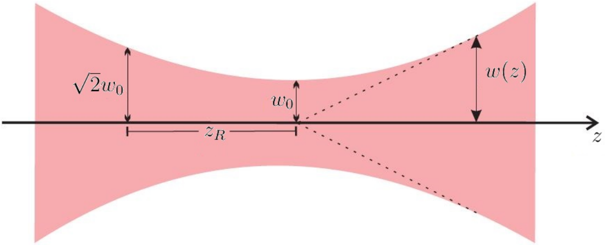

Figura 2 – Lateral view of a Gaussian beam propagating along z.

Substituting equations (2.19) - (2.21) into equation (2.18), we obtain the expression for the complex amplitude of the Gaussian beams

$$C(\boldsymbol{x},\boldsymbol{y},\boldsymbol{z}) = c_0\frac{w_0}{w(z)}e^{-ik\left(\frac{x^2+y^2}{2R(z)}\right)}e^{-\left(\frac{x^2+y^2}{w^2}\right)}e^{i\Phi(z)}\ , \tag{2.22}$$

where $\Phi(z)$ is defined as

$$\Phi(z) = \tan^{-1}\left(\frac{z}{z_R}\right)\ , \tag{2.23}$$

and is called Gouy phase.

2.1.3 Hermite-Gaussian Beams

The paraxial Helmholtz equation can be solved in many different ways, and using different coordinate systems. A typical solution in Cartesian coordinates gives a family of functions describing the so called Hermite-Gaussian beams (SVELTO, 1976). They possess rectangular symmetry in the transverse plane and their complex amplitudes can be written as

$$HG(\boldsymbol{x},\boldsymbol{y},\boldsymbol{z})_{mn} = c_{mn}\frac{w_0}{w(z)}H_m\left(\frac{\sqrt{2}x}{w(z)}\right)H_n\left(\frac{\sqrt{2}y}{w(z)}\right)e^{-\left(\frac{x^2+y^2}{w(z)^2}\right)}e^{i(m+n+1)\Phi(z)}e^{-i} \tag{2.24}$$

where H_m and H_n are the Hermite polinomials defined as

$$H_im(x) = (-1)^m e^{x^2}\frac{d^m}{dx^m}e^{-x^2}. \tag{2.25}$$

Some normalized intensity profiles for the first few orders are shown in Fig. 3, where $m = n = 0$ is a Gaussian beam, presented in the previous section.

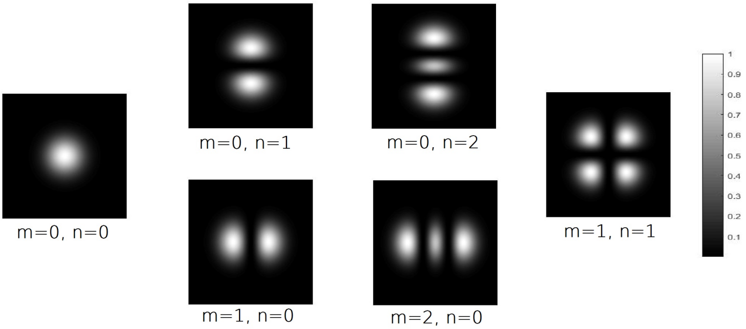

Figura 3 – Typical normalized intensity profiles for some Hermite-Gaussian modes.

2.1.4 Laguerre-Gaussian beams

For the present work, the most relevant solutions to equation (2.17) are the Laguerre-Gaussian beams (ALLEN et al., 1992). They are the solution to the paraxial wave equation in cylindrical coordinates, so that they possess rotational symmetry around their axis of propagation and carry orbital angular momentum of $\ell\hbar$ per photon (PADGETT; ALLEN, 2000). The orbital angular momentum of a light beam is a discrete degree of freedom and we will use it to study a quantum thermodynamics protocol. These solutions can be obtained by writing the paraxial Helmholtz equation in cylindrical coordinates (ρ, ϕ, z). Their complex amplitude can be written in terms of the cylindrical coordinates (ρ, ϕ, z) as

$$\begin{aligned} LG_{p\ell}(\rho,\phi,z) = & c_{p\ell}\frac{w_0}{w(z)}\left(\frac{\sqrt{2}\rho}{w(z)}\right)^{|\ell|} L_p^{|\ell|}\left(\frac{2\rho^2}{w^2(z)}\right)\exp\left(-\frac{\rho^2}{w^2(z)}\right) \\ & \exp\left(-i\left(\frac{k\rho^2}{2R(z)} + \left(2p+|\ell|+1\right)\Phi(z)\right)\right)\exp\left(-i\ell\phi\right), \end{aligned} \tag{2.26}$$

where L_p^ℓ are the Laguerre polynomials, defined as

$$L_p^\ell(x) = \frac{x^{-p}e^{x}}{\ell!}\frac{d^\ell}{dx^\ell}\left(e^{-x}x^{\ell+p}\right). \tag{2.27}$$

The other variables have been defined in equations (2.20), (2.21) and (2.23).

For these solutions p and ℓ are the radial and the azimuthal indices, respectively. The normalized intensity profiles of some orders of Laguerre-Gaussian modes are shown in Figure 4. Again the Gaussian mode is a special case of a Laguerre-Gaussian mode for $p = \ell = 0$, making it a common element of the Hermite and Laguerre-Gaussian bases.

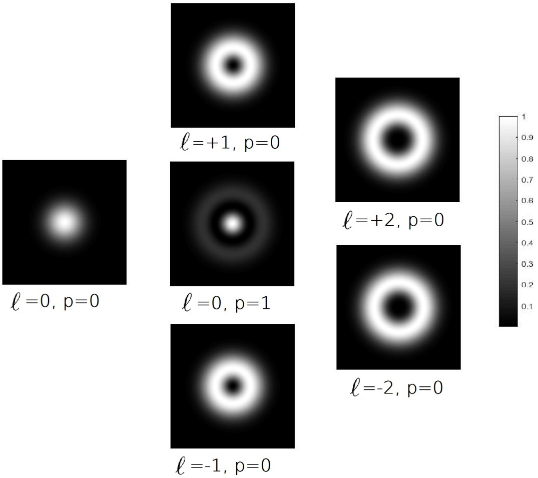

ℓ=+1, p=0

ℓ=+2, p=0

ℓ=0, p=0

ℓ=0, p=1

ℓ=-2, p=0

ℓ=-1, p=0

Figura 4 – Normalized intensity profiles of Laguerre-Gaussian modes.

2.2 PRODUCTION OF LAGUERRE-GAUSSIAN BEAMS

2.2.1 Holograms

Among several possible methods for generating Laguerre-Gaussian light beams, we have chosen to use holograms. The reason for this choice is that we can create holograms with a Spatial Light Modulator

(SLM) with high versatility using a computer interface, a device that will be explained in detail in chapter 4.2. SLMs are reflecting panels that can modulate the phase of the incident light in a controlled way. We will describe it in more detail later. In Holography, also referred to as the method of reconstructing wavefronts, a diffraction screen called hologram can be used to rebuild the light field that is reflected or emitted by an object.

A laser beam, for instance, is split into two identical parts. One beam hits an object and is reflected onto a photographic film and the second beam, the reference beam, hits the film directly. By being exposed to the reflected beam and reference beam at the same time, an interference pattern will be recorded on the photographic film, which is the hologram. The production of the hologram is shown in Fig. 5 a). This interference pattern has all the information necessary to reproduce the light field reflected by the object. This means that if the hologram is now illuminated with the same laser beam - the reference beam - the resulting diffraction will be exactly a copy of the beam that was reflected by the object (Fig. 5 b)).

For our purpose, the object to be reconstructed corresponds to a Laguerre-Gaussian beam and the reference beam is a Gaussian beam from a laser source. The Gaussian laser beam can be approximated by a plane wave in a simplified approach, while a more detailed description may be necessary in some cases. A resulting diffraction pattern (hologram) of those two beams can be seen in Figure 6 . This interference pattern will be calculated computationally later.

This hologram acts like a diffraction grating, where the zero order maximum coincides with the laser beam maximum and the diffraction maxima of order m for a single forked hologram possess an orbital angular momentum $\ell = m$.

We are interested in the diffracted beams with orbital angular momentum. More specifically, for each desired value of orbital angular momentum ℓ, we calculate the hologram so that the first order maximum has the desired amplitude and phase distribution.

This hologram pattern can be realized in a binary fashion. This means that for a phase difference between 0 and π the transmission is zero (black) and for a phase difference between π and 2π the transmission is set to be unity (white). The relative intensities of the two interfering beams play no role. In this way, only a limited amount of the incident power is coupled to the first order maximum. However, it is possible to increase the power coupling to the first order by replacing the binary hologram with a continuous one called blazed diffraction

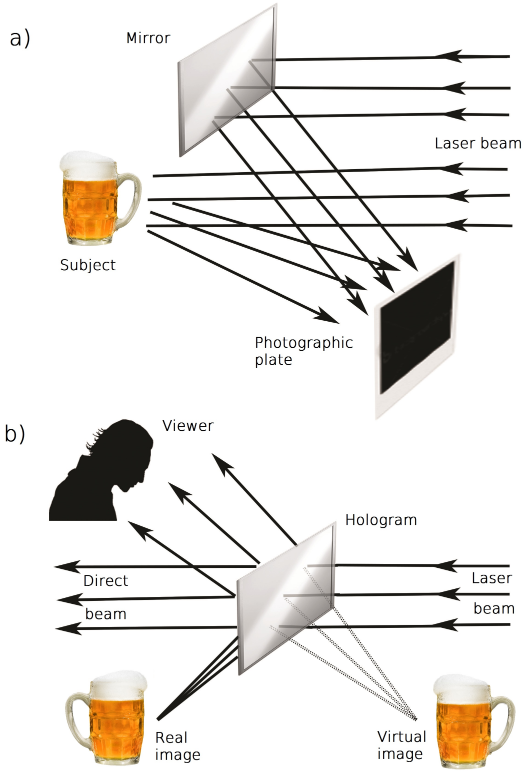
a)
Mirror
Laser beam
Subject
Photographic
plate
b)
Viewer
Hologram
Direct
beam
Laser
beam
Real
image
Virtual
image

Figura 5 – a) Arrangement for producing a hologram; b) use of the hologram in producing the real and virtual images.

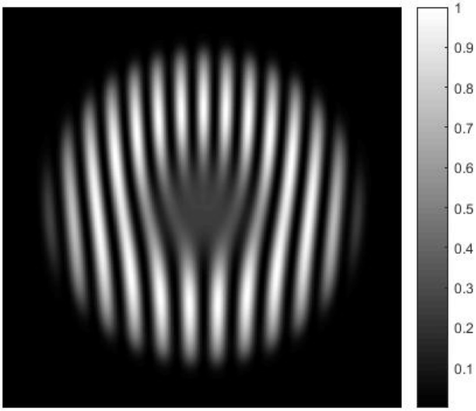

Figura 6 – Simulation of an interference pattern of a Laguerre-Gaussian beam ($\ell = 3,\ p = 0$) and a plane wave.

grating.

We have implemented blazed diffraction gratings to generate Laguerre-Gaussian beams using Spatial Light Modulators (SLM). As a matter of fact, the light beams we produce are not exactly Laguerre-Gaussian beams since we have used a simpler version of the hologram showed in Fig. 6. The holograms we use are not modulated by the doughnut-like shape of the LG mode as we will see in section 4.2. However, the key issue for us is that we are able to produce light beams with controlled orbital angular momentum.

3 QUANTUM THERMODYNAMICS AND SIMULATION WITH CLASSICAL LIGHT

3.1 SIMULATION OF A QUANTUM HARMONIC OSCILLATOR WITH CLASSICAL LIGHT

In this work we present the theory and the experimental implementation for simulating a quantum harmonic oscillator with light beams and using it to investigate quantum aspects of thermodynamics. With our experiment we introduce a new platform to study thermodynamical aspects of high dimensional quantum systems. Out-of-equilibrium thermodynamics of quantum systems has helped to gain further insights on the thermodynamics of small systems under external perturbations (ESPOSITO; HARBOLA; MUKAMEL, 2009; CAMPISI; HÄNGGI; TALKNER, 2011).

While the experimental study of the classical domain showed promising success, the quantum mechanical regime needs the employment of the statistics of work performed onto or by a driven quantum system. This has been shown to be a hard task, due to difficulties in the implementation of reliable projective measurements of energy eigenstates (CAMPISI; HÄNGGI; TALKNER, 2011; HEYL; KEHREIN, 2012), as it has been proven that work is not an observable in quantum systems (TALKNER; LUTZ; HÄNGGI, 2007). However, there are a few proposals to overcome this difficulty (HUBER et al., 2008; HEYL; KEHREIN, 2012; PEKOLA et al., 2013) and progress has been made with approaches based on an interferometric scheme in which the information about the energy is encoded in phases of an electromagnetic field and measured with interference (DORNER et al., 2013; MAZZOLA; CHIARA; PATERNOSTRO, 2013; CAMPISI et al., 2013). The most promising progress has been made by Batalhão *et al.* (ref. (AO et al., 2014)), as they present the experimental reconstruction of the nonequilibrium work probability distribution in a closed quantum system, using a liquid-state nuclear magnetic resonance platform.

Here, we adopt the so called two-measurement approach, where the projections onto the energy eigenstates are made directly. We use Laguerre-Gaussian light beams to emulate the energy eigenstates of a quantum harmonic oscillator and a Spatial Light Modulator to drive the system out of equilibrium. We show that the scheme can be implemented in a well controlled way, and the measurements can be properly realized in certain circumstances.

3.2 SIMULATION SCHEME

Our simulation of a quantum system using classical light is possible due to the analogy between the paraxial wave equation and the Schrödinger equation. If we replace the coordinate z in equation (2.17) with the time variable, it takes the same form as the Schrödinger equation for a free particle in two dimensions (GLOGE; MARCUSE, 1969).

The formalism of quantum mechanics, which includes a Hilbert space and linear operators can be directly transferred to a classical light beam under the paraxial approximation (STOLER, 1981). It has been shown that Hermite-Gaussian and Laguerre-Gaussian beams emulate the energy eigenstates of a two-dimensional quantum harmonic oscillator (ALLEN et al., 1992; NIENHUIS; ALLEN, 1993) and the quantum limit of a chaotic harmonic oscillator has been investigated experimentally using this analogy (LEMOS et al., 2012).

The Laguerre-Gaussian optical modes used in our work simulate the two-dimensional quantum harmonic oscillator (QHO) in such a way that the transverse distribution of the electric field has the same form as the energy eigenfunctions of the 2-D QHO. Performing the simulation of the quantum system in this way, it accounts for the oscillatory aspects like state superposition, coherence and decoherence. The photonic quantum properties of light itself do not come into play here, because we are solely interested in the modal structure of the created beams.

3.2.1 Qantum harmonic oscillator formalism

Using the ladder operator method with annihilation and creation operators

$$a = \sqrt{\frac{m\omega}{2\hbar}}\left(\hat{x} + \frac{i}{m\omega}\hat{p}\right) \;; \tag{3.1}$$

$$a^{\dagger} = \sqrt{\frac{m\omega}{2\hbar}}\left(\hat{x} - \frac{i}{m\omega}\hat{p}\right) \;, \tag{3.2}$$

where $\hat{x}$ and $\hat{p}$ are the position and momentum operators, one can define the number operator N with its eigenvalues n.

$$N = a^\dagger a \tag{3.3}$$

$$N|n\rangle = n|n\rangle \ , \tag{3.4}$$

where $|n\rangle$ are the energy eigenstates of the Hamiltonian. For the 2D QHO, the Hamiltonian H and the angular momentum operator L_z form a complete set of commuting observables.

In the same fashion we can define the right and left circular ladder operators.

$$a_r = \frac{1}{\sqrt{2}}(a_x - ia_y) \tag{3.5}$$

$$a_l = \frac{1}{\sqrt{2}}(a_x + ia_y) \ . \tag{3.6}$$

If we use the number operators for right and left circular quanta, $N_r = a_r^\dagger a_r$ and $N_l = a_l^\dagger a_l$ respectively, we can write the Hamiltonian as

$$H = (N_r + N_l + 1)\hbar\omega \ , \tag{3.7}$$

with eigenvalues given by

$$\varepsilon_{\ell p} = (|\ell| + 2p + 1)\hbar\omega \ . \tag{3.8}$$

The angular momentum operator can also be written in terms of these operators:

$$L_z = (N_r - N_l)\hbar \tag{3.9}$$

with eigenvalues

$$\lambda_\ell = \hbar\ell \ . \tag{3.10}$$

Here ℓ is the azimuthal and p the radial quantum number. These are the analogous to the azimuthal and radial indices that were introduced in eq. (2.26) in the derivation of the expression for the Laguerre-Gaussian beams, leading us to the analogy between the field profile of the Laguerre-Gaussian beams and the 2D wave functions of the QHO.

Now, if we look at the subset of states where $p = 0$, which is always the case when, for example either N_r or N_l has the eigenvalue zero, then the energy eigenvalues are simplified to

$$\varepsilon_\ell = (|\ell| + 1)\hbar\omega \ . \tag{3.11}$$

For this special case, the energy and the angular momentum are directly related. This means that a projection in the OAM basis is equivalent to a projection in the energy eigenbasis.

3.3 THERMAL STATES

In our simulation scheme we prepare and measure the energy eigenstates $|n\rangle$ of the QHO, where $n = |\ell|$ in Eq. (3.11). Those states are also referred to as Fock states or number states. Using the creation operator, one can define those number states as follows:

$$a^\dagger|n\rangle = \sqrt{n+1}|n+1\rangle \ ; \tag{3.12}$$

$$|n\rangle = \frac{(a^\dagger)^n}{\sqrt{n!}}|0\rangle \ , \tag{3.13}$$

with the vacuum state $|0\rangle$.

For our experiment we want our system to be initially in a thermal state. We can now use those number states, which we are able to produce in the analogy of our simulation scheme, to define a thermal state.

A thermal state in Quantum Optics is a state that is produced by a thermal source. A heated body in thermal equilibrium at a temperature T emits electromagnetic radiation. This radiation is called *thermal radiation* or *chaotic radiation.* A thermal light source that makes use of this property is for example a light bulb. Apart from the emissivity, thermal radiation from a real source is equal to the black body radiation and the emissivity is not relevant in the context of our problem. A black body radiates a continuous spectrum of frequencies over a wide range. The spectrum and the radiated energy depend on the temperature of the surface of the body. This relation is described by *Planck's law of black body radiation* (PLANCK, 1910; BOSE; EISNTEIN, 1924)

$$B_\nu(T) = \frac{2h\nu}{c^3}\frac{1}{e^{\frac{h\nu}{k_B T}} - 1} \ , \tag{3.14}$$

where $B_\nu(T)$ is the spectral radiance, h is the Planck constant, c is the speed of light, k_B is the Boltzmann constant, ν is the frequency of radiation and T is the absolute temperature of the body. Furthermore, for fixed temperatures the radiated power for different frequencies varies and the frequency of the maximum radiation power is found to be proportional to the absolute temperature. This relation between the spectra of black body radiation for different temperatures is known as *Wien's displacement law*. The overall power of radiation is found to increase with the fourth power of the absolute temperature and is expressed by the *Stefan-Boltzmann law*. The radiation emitted by a black body is spread into several electromagnetic modes. These modes can be described in terms of plane waves and they are characterized by a wave vector $\vec{k}$ and a frequency ν. These modes are called *thermal states* and in the optical regime, we call them *optical modes*. We can isolate one optical mode by spatial filtering and filtering one single frequency, for example. The radiated energy of each mode is quantized, as the energy of photons is determined by their frequency and just a finite amount of photons occupy each mode. The average number of photons that occupy one optical mode from a thermal source is given by (BOSE; EISNTEIN, 1924):

$$\langle n_\nu \rangle = \frac{1}{e^{\frac{h\nu}{k_B T}} - 1} \ . \tag{3.15}$$

This relation is known as the *Bose-Einstein distribution law for photons*. All the properties of thermal radiation depend on the absolute temperature of the radiating body and are heavily subjected to fluctuations. Therefore a thermal state is defined just by its statistical nature.

As a thermal state is not a pure state we can write it as a density matrix:

$$\rho = \sum_n p(\varepsilon_n)|n\rangle\langle n| \ , \tag{3.16}$$

where $p(\varepsilon_n)$ is the probability to detect exactly n photons in the optical mode with frequency ν. By using the average photon number this probability distribution can be expressed as (WALLS, 1994):

$$\begin{aligned} p(\varepsilon_n) &= \frac{\langle n\rangle^n}{(1+\langle n\rangle)^{n+1}} \\ &= e^{\left(\frac{-\varepsilon_n}{k_B T}\right)^n}\left(1 - e^{\frac{-\varepsilon_n}{k_B T}}\right) \\ &= \frac{e^{\frac{-\varepsilon_n}{k_B T}}}{\sum\limits_n e^{\left(\frac{-\varepsilon_n}{k_B T}\right)}} \\ &= \frac{e^{-\beta\varepsilon_n}}{Z}, \end{aligned} \tag{3.17}$$

where Z is called the partition function and we used $\beta = 1/k_B T$.

3.3.1 Simulation of thermal states

To come back to the analogy with the Laguerre-Gaussian beams containing OAM, we just substitute the number states $|n\rangle$ with the Laguerre-Gaussian states $|\ell\rangle$ and the energy eigenvalues are given by Eq. (3.11).

Since the states $|\ell\rangle$ and $|-\ell\rangle$ have the same energy, their probabilities ($p(\varepsilon_\ell) = p(\varepsilon_{-\ell})$) are the same. Because of this, every energy level has degeneracy 2, except the ground state $\ell = 0$.

By using the definition of our thermal state and the fact that the diagonal elements need to sum to 1 we can derive a expression for the partition function Z, which is defined as the sum of the Boltzmann factors $e^{-\beta\varepsilon_n}$ for all states, as follows:

$$\begin{aligned} \sum_{\ell=-\infty}^{+\infty} p(\ell) = 1 \qquad \qquad \qquad \qquad \qquad \qquad \qquad \qquad \qquad \qquad \qquad (3.18) \\ = \frac{1}{Z}\left(e^{-\beta\hbar\omega} + 2e^{-2\beta\hbar\omega} + 2e^{-3\beta\hbar\omega} + ...\right) \\ = \frac{2}{Z}\underbrace{\left(e^{-\beta\hbar\omega} + e^{-2\beta\hbar\omega} + ...\right)}_{=S} - \frac{e^{-\beta\hbar\omega}}{Z} \end{aligned}$$

We can rewrite the sum S using the following relation

$$
\begin{aligned}
e^{-\beta\hbar\omega}\ S &= S - e^{-\beta\hbar\omega} \\
\Leftrightarrow S &= \frac{e^{-\beta\hbar\omega}}{1-e^{-\beta\hbar\omega}}
\end{aligned}
\tag{3.19}
$$

$$
\begin{aligned}
\Rightarrow 1 &= \frac{1}{Z}\left(2\frac{e^{-\beta\hbar\omega}}{1-e^{-\beta\hbar\omega}} - e^{-\beta\hbar\omega}\right) \\
&= \frac{e^{-\beta\hbar\omega}}{Z}\left(\frac{2}{1-e^{-\beta\hbar\omega}} - 1\right) \\
&= \frac{e^{-\beta\hbar\omega}}{Z}\left(\frac{1+e^{-\beta\hbar\omega}}{1-e^{-\beta\hbar\omega}}\right) \\
&= \frac{e^{-\beta\hbar\omega}}{Z}\left(\frac{e^{\frac{-\beta\hbar\omega}{2}}}{e^{\frac{-\beta\hbar\omega}{2}}}\left(\frac{e^{\frac{\beta\hbar\omega}{2}}+e^{\frac{-\beta\hbar\omega}{2}}}{e^{\frac{\beta\hbar\omega}{2}}-e^{\frac{-\beta\hbar\omega}{2}}}\right)\right) \\
&= \frac{e^{-\beta\hbar\omega}}{Z}\frac{1}{\tanh\frac{\beta\hbar\omega}{2}}
\end{aligned}
$$

$$
\Rightarrow Z = \frac{1}{e^{\beta\hbar\omega}\tanh\frac{\beta\hbar\omega}{2}}\ . \tag{3.20}
$$

With this, our thermal probability weights are determined by:

$$
p(\ell) = \frac{e^{-\beta\varepsilon_\ell}}{Z} = e^{-\beta(|\ell|+1)\hbar\omega}e^{\beta\hbar\omega}\tanh\frac{\beta\hbar\omega}{2} \tag{3.21}
$$

Using this result to substitute $p(\varepsilon_n)$ in Eq. (3.16) and substituting the number states $|n\rangle$ for the OAM states $|\ell\rangle$, our thermal states are well-defined.

3.4 WORK DISTRIBUTION

Now that we defined thermal states in terms of $|\ell\rangle$ and each state has the energy $\big(|\ell|+1\big)\,\hbar\omega$, we can define work in our system.

Work is defined as the difference between two energy measurements. One measurement before the process and one after a considered process took place. In our approach the work done on or by the system depends only on the change in $|\ell|$. We can write the work for a process from an initial ℓ to a final ℓ' as

$$W_{\ell\ell'} = (|\ell'| - |\ell|)\hbar\omega \ . \tag{3.22}$$

Using this definition, the work probability distribution becomes

$$P(W) = \sum_{\ell,\ell'} p_{\ell\ell'} \ \delta(W - W_{\ell\ell'}) \ , \tag{3.23}$$

where $p_{\ell\ell'}$ is the probability of observing the transition $\ell \to \ell'$, given by:

$$p_{\ell\ell'} = p_{\ell} p_{\ell'|\ell} \ , \tag{3.24}$$

where p_{ℓ} is the probability of obtaining the angular momentum ℓ as a result for the first projective measurement [given by Eq. (3.17)] and $p_{\ell'|\ell}$ is the conditional probability of ending up with angular momentum ℓ' given that the system was initially with angular momentum ℓ.

3.5 JARZYNSKI THEOREM

We want to study thermodynamical aspects of the simulated quantum system.
Fluctuation theorems are relations that provide information about the thermodynamics of small systems in the non-equilibrium regime for short time scales, when fluctuations come into play. By taking into account fluctuations in nonequilibrium dynamics, they connect properties of thermodynamical equilibrium with explicit nonequilibrium features. In this work we will evaluate the Jarzynski fluctuation theorem for a given process.

Every fluctuation relation starts with two parts; the initial state of the system and the principle of microreversibility (HOROWITZ; JARZYNSKI, 2007). The system under study is supposed to be in thermal equilibrium and can therefore be described by its statistical properties, like the thermal states that have been defined in section 3.3. Here, microreversibility is concerned with systems described by explicitly time-dependent Hamiltonians.

We consider a system described by the coordinates $\mathbf{q}$ and the conjugate momenta $\mathbf{p}$, and $z = (\boldsymbol{q}, \boldsymbol{p})$ is a point in its phase space. The system shall be driven by an external force X_t. The time-dependent

Hamiltonian then reads

$$H(z, X_t) = H_0(z) - X_t \alpha(z) \ , \tag{3.25}$$

where α is the coordinate conjugate to the external force X and H_0 is the energy of the system without an external perturbation. For simplicity, we assume the Hamiltonian to be time-reversal-invariant for fixed values of X,

$$H(z^*, X) = H(z, X) \ . \tag{3.26}$$

The reversal of momentum $\boldsymbol{p} \rightarrow -\boldsymbol{p}$ is denoted by the asterix.

Our system is prepared in a thermal state at equilibrium at the inverse temperature $\beta = 1/k_B T$, as explained in section 3.3 (the experimental realization will be discussed in the next chapter). Now, the system evolves from $t = 0$ to τ according to the Hamilton equations, when the external force is applied according to the protocol X_t. The trajectory in phase space from $t = 0$ to τ is denoted by γ. Now we want to consider two processes, which we call *forward* (F) and *reverse* (R). For the forward process the external force goes from $X_0^F = A$ to $X_\tau^F = B$ and for the reversed process from B to A, with the time-reversed protocol

$$X_t^R = X_{\tau - t}^F \ . \tag{3.27}$$

This means that the backwards process is the time-reversed forward process (ESPOSITO; HARBOLA; MUKAMEL, 2009).

After the protocol is applied, the system again thermalizes and returns to a thermal state. Considering the assumption of time-reversal invariance, every forward trajectory γ^F comes with a conjugate reverse trajectory γ^R (figure 7) where

$$z_t^R = z_{\tau - t}^{F*} \ . \tag{3.28}$$

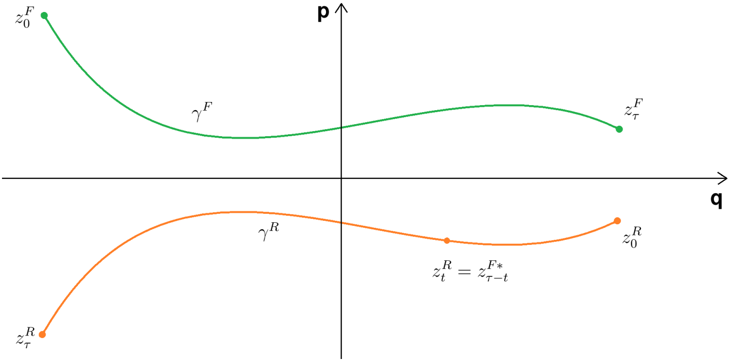

Figura 7 – Schematic illustration of the forward trajectory (green) and its conjugate reversed trajectory (orange), with the relation of reversed momenta and time between them according to equation (3.28).

For every realization of the process X to the prepared system, we generate an independent sample of a trajectory $(\gamma_1, \gamma_2, ...)$, so that we obtain a probability distribution $P[\gamma]$, with a probability $P[\gamma_i]$ to observe a certain trajectory γ_i. Crooks then arrived at the following expressions for forward and reversed processes (CROOKS, 1998)

$$P_F[\gamma^F] = \frac{1}{Z(A)} \exp\left[-\beta H(z_0^F, A)\right] \ ; \tag{3.29}$$

$$P_R[\gamma^R] = \frac{1}{Z(B)} \exp\left[-\beta H(z_0^R, B)\right] \ , \tag{3.30}$$

where

$$Z(X) = \int dz \ e^{-\beta H(z,H)} \tag{3.31}$$

is the partition function.
This leads to the relation

$$\frac{P_F[\gamma^F]}{P_R[\gamma^R]} = e^{-\beta \Delta F} e^{\beta [H(z_0^R, B) - H(z_0^F, A)]} \ , \tag{3.32}$$

where the definition for the free energy was used.

$$\begin{aligned} F(X) =& \frac{\ln\, Z(X)}{-\beta} && (3.33)\\ \Rightarrow \Delta F =& F(B) - F(A) \\ =& -\beta\, \ln \frac{Z(B)}{Z(A)}\ . && (3.34) \end{aligned}$$

With the definition of work (CROOKS, 1998; JARZYNSKI, 1997)

$$\begin{aligned} W =& H(z_\tau^F, B) - H(z_0^F, A) \\ =& H(z_0^R, B) - H(z_0^F, A)\ , && (3.35) \end{aligned}$$

this leads to the final expression (CROOKS, 1998):

$$\frac{P_F[\gamma^F]}{P_R[\gamma^R]} = e^{\beta(W-\Delta F)}\ . \tag{3.36}$$

From this result follows the Crooks fluctuation theorem, that connects the forward and reverse work distributions (CROOKS, 1999):

$$\frac{\rho_F(W)}{\rho_R(-W)} = e^{\beta(W-\Delta F)}\ . \tag{3.37}$$

If we multiply both sides of equation (3.37) by $\rho_R(-W)e^{-\beta W}$ and integrate over W we get the Jarzynski equality (JARZYNSKI, 1997):

$$\langle e^{-\beta W} \rangle = e^{-\beta \Delta F}\ . \tag{3.38}$$

To apply these relations to quantum systems, a quantum mechanical definition of work is necessary. In earlier works a work operator has been defined, which led to quantum corrections, as the final Hamiltonian does not commute with the initial Hamiltonian. This is due to the fact that work is not a quantum observable (TALKNER; LUTZ; HÄNGGI, 2007). However the Jarzynski equation holds for quantum systems, by defining work as the difference between an initial and a final projective energy measurement of the system (ESPOSITO; HARBOLA; MUKAMEL, 2009).

ENTROPY PRODUCTION

Fluctuation relations can be connected to entropy production. With the definitions

$$S = -\mathrm{Tr}\rho(t)\ \ln\ \rho(t) = -\mathrm{Tr}\rho(0)\ \ln\ \rho(0) \quad \text{and} \tag{3.39}$$

$$\bar{S} = -\mathrm{Tr}\rho(t)\ \ln\ \rho^R(0) = -\mathrm{Tr}\rho(0)\ \ln\ \rho^R(t)\ , \tag{3.40}$$

and setting the initial density matrices for the forward and reverse process as

$$\rho(0) = \frac{e^{\beta H(0)}}{Z(0)} \quad \text{and} \tag{3.41}$$

$$\rho^R(0) = \frac{e^{\beta H(t)}}{Z(t)}\ , \tag{3.42}$$

we get

$$\bar{S} - S = \beta\left(\langle W\rangle - \Delta F\right) \geq 0\ . \tag{3.43}$$

This means that because $\langle W\rangle$ is the average work, $(\bar{S} - S)\beta^{-1}$ is the irreversible work.

Since S can be identified as an entropy, $(\bar{S} - S)$ is the irreversible contribution to the entropy change. So this can be seen as the entropy production for the realization of a process that takes an initial probability distribution $\rho(0)$ and changes it to the final distribution $\rho(\tau)$ (CROOKS, 1999).

If we consider a linear map $\Phi\ :\ \mathcal{M}(\mathcal{H}_A) \to \mathcal{M}(\mathcal{H}_B)$, where $\mathcal{M}(\mathcal{H})$ denotes the space of linear operators on a finite-dimensional Hilbert space $\mathcal{H}$, then we can express any process in the operator-sum representation:

$$\Phi(X) = \sum_\mu K_\mu X K_\mu^\dagger\ , \tag{3.44}$$

where $X \in \mathcal{M}(\mathcal{H}_A)$ and K_μ are Kraus operators (KRAUS, 1983). For any physical process this map has to be completely positive. If a process fulfills the equation

$$\Phi(\mathbb{1}_A) = \sum_\mu K_{mu} K_\mu^\dagger = \mathbb{1}_B\ , \tag{3.45}$$

it is called a *unital* process (NIELSEN; CHUANG, 2011). This means the process preserves the identity. E. g. depolarizing channel and phase damping channel are unital, whereas the amplitude damping channel is not (NIELSEN; CHUANG, 2011). All processes in the experiments presented in this work are unital processes. With the definition of the entropy production $\sigma = \beta\,(W - \Delta F)$, we can write the fluctuation theorem for unital processes as

$$\langle e^{-\sigma} \rangle = 1 \; , \tag{3.46}$$

It has been proven that the Jarzynski's relation holds for unital process (RASTEGIN, 2013) and even for arbitrary quantum operations (RASTEGIN; ZYCZKOWSKI, 2014).

3.6 MUTUAL INFORMATION AND MAXWELL‘S DEMON

In our experiments we want to study thermodynamical processes that include a feedback control, called a Maxwell's demon. The expression *Maxwell's demon* comes from the famous *Gedankenexperiment*, where a little *demon* is able to extract information about the microscopic state of a gas and uses this information to divide fast and slow particles into two separate chambers. This is a violation of the second law of thermodynamics as it decreases the entropy of the system. Such an action of a Maxwell's demon can be characterized by the mutual information between a system and a feedback control mechanism. The scheme of a measurement feedback control mechanism is illustrated in Fig. 8.

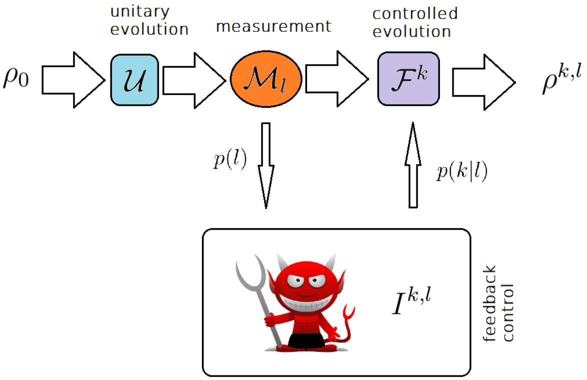

Figura 8 – Illustration of the action of a Maxwell's demon. After the system initially in state ρ_0 is driven unitarily ($\mathcal{U}$), the demon uses the outcome l of the measurement $\mathcal{M}_l$ to apply a controlled evolution $\mathcal{F}^k$.

Let us consider a system in the equilibrium state ρ_0 which is unitarily driven ($\mathcal{U}$) to a non-equilibrium state. If the demon performs a projective measurement $\mathcal{M}_l$ of the system, yielding the outcome l with probability $p(l)$ then a feedback control can use the information of the outcome of the measurement to apply a feedback evolution $\mathcal{F}^k$ to the system, leaving the system in the state $\rho^{k,l}$. The controlled evolution is performed correctly with probability $p(k|l)$, where $p(k|l)$ is the conditional probability of applying the evolution $\mathcal{F}^k$ given that the result of the measurement was l. This probability characterizes the measurement error of the feedback measurement and can account for noise for example. For a suitable choice of the operations $\{\mathcal{F}^k\}$, the feedback control mechanism can decrease the entropy production rate produced by the initial unitary operation $\mathcal{U}$. The amount of entropy the demon can reduce by extracting information is determined by the mutual information I between the system and the feedback control mechanism. If a measurement yields the outcome l and the demon applied the evolution $\mathcal{F}^k$ the extracted information is (SAGAWA; UEDA, 2010):

$$I(k,l) = \ln \frac{p(k|l)}{p(k)} \,, \tag{3.47}$$

where $p(k) = \sum_l p(k|l)p(l)$. This gives the average mutual information as (SAGAWA; UEDA, 2010):

$$\langle I \rangle = \sum_{k,l} p(k|l)p(l)I(k,l) \tag{3.48}$$

For example the demon can extract one bit of information, e.g. the sign of an observable (negative [-] or positive [+]), and always applies the correct controlled evolution $\mathcal{F}^k$ without errors, which means $p(\pm|\pm) = 1$. Then the probability of applying $\mathcal{F}^+$ or $\mathcal{F}^-$ is

$$p(\mathcal{F}^+) = p(\mathcal{F}^-) = \sum_{l} p(\pm|l)p(l) = 1 * 0.5 \ + \ 0 * 0.5 = 0.5 \ . \tag{3.49}$$

Then with

$$\begin{aligned} I^{\pm,\pm} &= \ln \frac{1}{0.5} = \ln 2 \\ I^{\pm,\mp} &= \ln \frac{0}{0} = \ln 1 = 0 \ , \end{aligned} \tag{3.50}$$

the average mutual information is

$$\langle I \rangle = \frac{1}{2} \ln 2 + \frac{1}{2} \ln 2 = \ln 2 \ . \tag{3.51}$$

Including the action of a Maxwell's demon and therefore the mutual information obtained by a feedback control, the Jarzynski's fluctuation relation can be written as (SAGAWA; UEDA, 2010; CAMATI et al., 2016):

$$\langle e^{-\beta(W-\Delta F)-I} \rangle = \langle e^{-\sigma-I} \rangle = 1 \ . \tag{3.52}$$

We can write the relation in Eq. (3.46) in the presence of a feedback control mechanism (Maxwell's Demon) as

$$\langle e^{-\sigma} \rangle = \gamma \ , \tag{3.53}$$

where γ now is a measure for the efficacy of the feedback control. For no feedback control at all we get $\gamma = 1$ and the relation reduces to the initial Jarzynski's relation from Eq. (3.46). When γ is large ($\gamma > 1$) we use extracted information to decrease the entropy of the system (SAGAWA; UEDA, 2010). This means the observation of the inequality

$$\langle e^{-\sigma} \rangle > 1 \ , \tag{3.54}$$

is evidence of a Maxwell's demon and a feedback control.

4 EXPERIMENT

We showed how Laguerre-Gaussian beams and their orbital angular momentum can be used to simulate a quantum harmonical oscillator and therefore to emulate a thermal state. In order to study thermodynamic aspects like the Jarzynski's fluctuation relation for this quantum system we want to apply a process to this system and reconstruct the work probability distribution of that given process by employing the projective measurement scheme. Here we present an experimental optical setup that provides a new platform for the experimental investigation of thermodynamic processes in the quantum regime.

4.1 EXPERIMENTAL SETUP

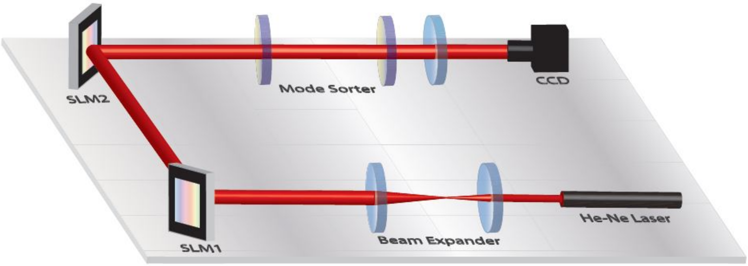

Figura 9 – Experimental setup: SLM1 creates input OAM modes from the expanded laser beam. SLM2 applies an action to the beam which is then analysed by a mode sorter.

The experimental setup is shown in Fig. 9. We use a He-Ne laser as a light source. The light beam is sent through two lenses with focal lengths $f_1 = 50\ mm$ and $f_2 = 300\ mm$, which are in a confocal arrangement. This results in an expansion of the beam by a factor of 6. Then the beam is sent to a Spatial Light Modulator (SLM), which is a device that imprints a phase transverse distribution in the light beams's wavefront. The spatial phase modulation is such that after some propagation, a light beam possessing orbital angular momentum is generated. These beams are practical approximations for the ideal

Laguerre-Gaussian beams, and are generated using forked holograms, as explained in section 2.2.1. Afterwards the beam is spatially modulated again by a second SLM (SLM2) which applies another phase mask.

Therefore SLM1 creates LG modes with OAM $\hbar\ell$ per photon, which are sent to SLM2, where an operation is applied to change the OAM according to a protocol. After the two operations have been performed the beam is directed to a device called *mode sorter* (BERKHOUT et al., 2010). This device sorts the OAM components of a beam along the horizontal axis which is afterwards recorded with a CCD camera. An example of recorded images can be seen in Fig. 10, where the horizontal intensity distribution of the image a) corresponds to the red line in Fig. 11 a) and the horizontal intensity distribution of the image b) corresponds to the green line in Fig. 11 a).

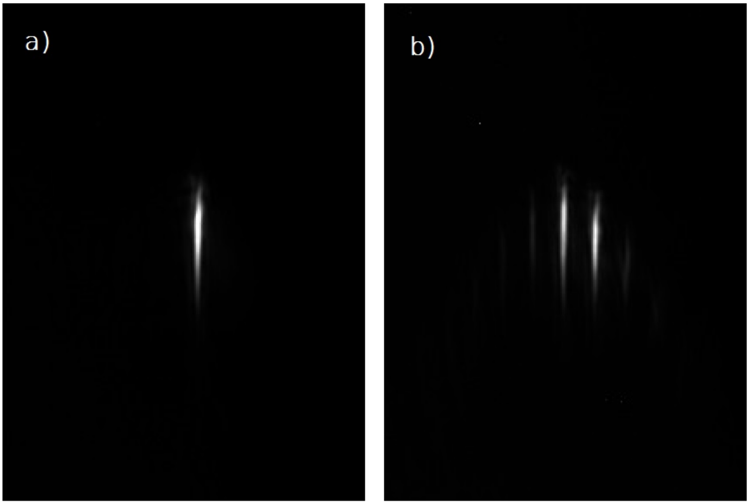

Figura 10 – Images recorded with a CCD camera after Laguerre-Gaussian beams passed through a mode sorter. The image in a) was recorded for a beam for $\ell = -7$ and the image in b) for a superposition of $\ell = -12$ and $\ell = -2$.

To calibrate this measurement scheme, SLM2 is used with no phase modulation so it acts as a mirror and SLM1 creates OAM modes of a given single ℓ one at a time. The intensity profiles of those modes are measured one by one after propagation through the mode sorter.

A plot of the calibration curves can be seen in Fig. 11, where each gray curve represents an input OAM mode and its horizontal intensity distribution on the CCD camera screen. Here the input was for values of ℓ ranging from -15 to 15. The red and green distributions in 11 a) where obtained from the recorded images in Fig. 10.

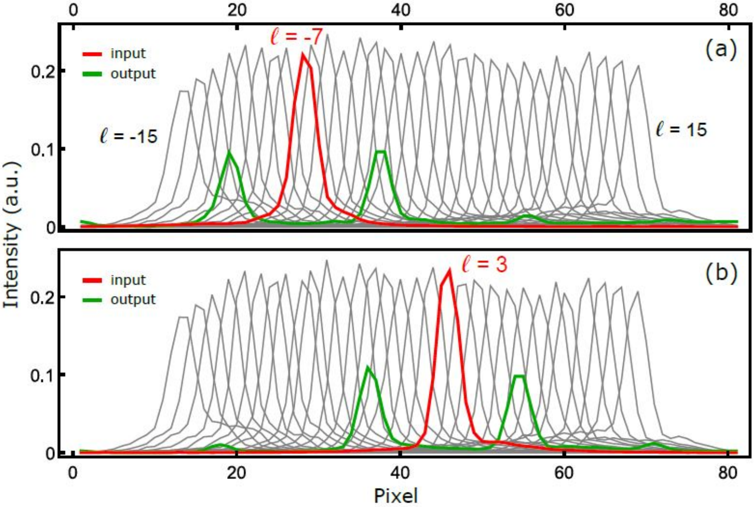

Figura 11 – Intensity distributions after the mode sorter when the process $(\mathcal{L}_{+5} + \mathcal{L}_{-5})/\sqrt{2}$ is applied to the input modes (a) $\ell = -7$ and (b) $\ell = 3$. In gray are the calibration curves for the input modes ranging from $\ell = -15$ to $\ell = +15$ without any process applied by SLM2.

The protocol is divided into two steps.

Step i of the protocol prepares a thermal state as described in chapter 3.3. This is done by sending a Gaussian mode (laser output mode) to SLM1. At the SLM1 a mask that generates OAM states with ℓ ranging from $-7 \leq \ell \leq 7$ is applied. The masks for different values of ℓ are applied randomly with probability p_ℓ [eq. (3.17)] over a time of 3 seconds each before they randomly change to another mask. The resulting beam is sent to SLM2, which acts as a mirror, and finally through the mode sorter and then to the CCD camera where the light intensity is measured. This measurement is a projective energy measurement in the initial Hamiltonian eigenbasis or, here equivalently, in the OAM basis with the assumption that the radial number p be equal to 0. A result for a measurement for one specific value of $\beta\hbar\omega$ is shown in Fig.

12. To create one thermal state like that in Fig. 12 the experiment as

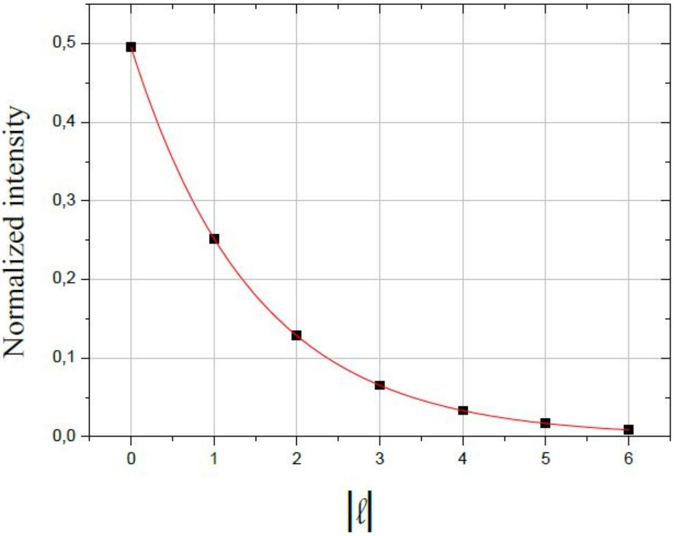

Figura 12 – Normalized intensity distribution as a function of $|\ell|$ for $\beta\hbar\omega = 0.67 \pm 0.01$.

explained in step *i* was run 300 times. The energy spectrum is discrete and infinite, yet, our input modes just range from $-7 \leq \ell \leq 7$. It is possible to produce thermal states within this range if we choose sufficiently low temperatures, so that the thermal weights corresponding to higher energies can be neglected and truncated. So far we prepared a thermal state and performed a projective energy measurement. However, in the second step of the protocol we want to perform an action on this state.

Step *ii* of the protocol performs an action on each separate input mode. The input modes are the 300 random modes prepared by SLM1 containing OAM ranging from $-7 \leq \ell \leq 7$, which represent one input thermal state. SLM2 then applies a phase mask which realizes the process whose work distribution we want to measure. These masks applied by SLM2 introduce OAM transitions as the input modes couple to other output OAM modes. Finally we are able to measure the OAM distribution using the mode sorter and the CCD camera. Comparing the measured distribution with the input thermal state we can reconstruct the work distribution of the applied process.

The process applied in the experiment is the linear operation

$$(\mathcal{L}_{+5} + \mathcal{L}_{-5})/\sqrt{2} \ , \tag{4.1}$$

where

$$\mathcal{L}_i|\ell\rangle = |\ell + i\rangle \ . \tag{4.2}$$

This means every input mode increases its OAM by 5 and decreases it by 5, each with a weight of $\frac{1}{2}$. A result for input modes $\ell = -7$ and $\ell = 3$ is shown in Fig. 11.

4.2 SPATIAL LIGHT MODULATOR

A spatial light modulator (SLM) is a device that imposes some sort of modulation on a beam of light. For example projectors are used to display computer monitor contents by modulating the intensity of a light beam. However, we are just interested in modulating the *phase* of our laser beam. In our experiment we are using the PLUTO-2 phase only Spatial Light Modulator manufactured by HOLOEYE (Fig. 13).

Figura 13 – Image of the SLM model PLUTO-2 by HOLOEYE.

It has a reflective liquid crystal on silicon microdisplay with a resolution of 1920x1080 pixels, where each pixel has a pitch of 8 μm. With appropriate calibration, each pixel can vary the phase of an incoming beam from 0 to 2π upon reflection by applying a 8-bit grayscale from 0 to 255.

We use the SLM to generate beams of light containing OAM (SLM1) and to vary the amount of OAM of the beam (SLM2). In order to generate a beam with OAM (Laguerre-Gaussian beams introduced in section 2.1.4), we use the method of holograms introduced in section 2.2.1. To calculate the hologram, the phase distribution of the Laguerre-Gaussian beam is added to a phase ramp and the sum of those is expressed as modulo 2π (YAO; PADGETT, 2011). An example is shown in Fig. 14. This generates a diffraction grating which creates the desired beam in the first order of diffraction. We manipulate the phase ramp with a technique called *blazing* to maximize the intensity output in the first order of diffraction (DAVIS et al., 1999).

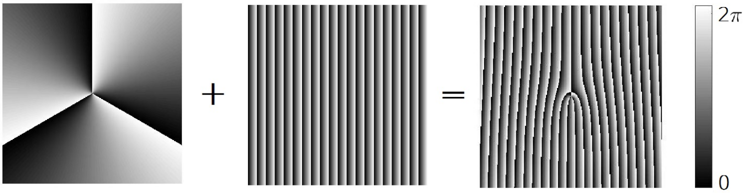

Figura 14 – Example for $\ell = 3$. Combination of the phase distribution and a phase ramp resulting in a forked diffraction grating.

These hologram masks are computed by a program written in *LabVIEW*, which is used to display them on the SLM as well.

The masks to change the OAM in a Laguerre-Gaussian beam are the same as the ones used to create the LG beams in the first place. For example, a mask that would generate a LG beam containing OAM of $\hbar\ell$ per photon from an initial Gaussian beam (laser beam) would change the OAM per photon of any LG beam by $\hbar\ell$.

4.3 MODE SORTER

The *mode sorter* is a device that implements geometric transformations in order to map different OAM modes onto different spatial regions. The method has been developed by Berkhout *et al.* (BERKHOUT et al., 2010). The mode sorter scheme is shown in Fig. 15. Because Laguerre-Gaussian beams possess an azimutal phase gradient, the first two optical elements of the mode sorter transform it into a horizontal phase gradient. As the LG modes have a doughnut-shaped intensity profile, one can think of this transformation as the mode sorter opening this circular shape into a horizontal band. The first optical element *opens* the mode and the second optical element provides a certain

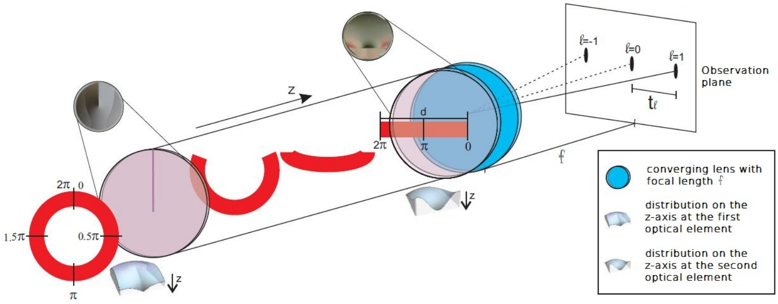
ℓ=-1
ℓ=0
ℓ=1
Observation plane
t_ℓ
z
d
2π
π
0
f
2π
0
1.5π
0.5π
π
z
z
converging lens with focal length f
distribution on the z-axis at the first optical element
distribution on the z-axis at the second optical element

Figura 15 – Illustration of the *mode sorter* scheme with the intensity of the beam in different planes along the axis of propagation for a LG mode ($\ell = 1$). Illustration taken from Ref. (ALMEIDA, 2015)

phase correction, so that the beam appears like a plane wave with a linear phase gradient. The third optical element is a converging lens. This lens realizes the optical Fourier Transform, so that the transverse phase gradient becomes a spatial displacement. Moreover, the light in the shape of a stripe becomes a thin vertical line in the Fourier plane. Examples of these recorded lines can be seen in Fig. 10. The specific position of this line determines the OAM of the incoming beam. An example of recorded images after Laguerre-Gaussian beams have passed a mode sorter can be seen in Fig. 10. Further explanations and calculations on the mode sorter have been done in portuguese language in chapter 4.4 of Ref. (ALMEIDA, 2015).

4.4 DETERMINATION OF THE ORBITAL ANGULAR MOMENTUM

As mentioned in the previous section, a Laguerre-Gaussian mode is turned into a thin line after passing through the mode sorter. The position of this line should determine the OAM of the incoming beam. We integrate the images recorded by the CCD camera along the vertical axis to get a marginal distribution of intensity along the horizontal axis. Examples of these intensity distributions are the calibration curves in Fig. 11, where an input mode for a single value of ℓ will result in a curve with one peak. This is illustrated in Fig. 16, where a single LG mode gives rise to one stripe in the left hand panels, and a superposition of

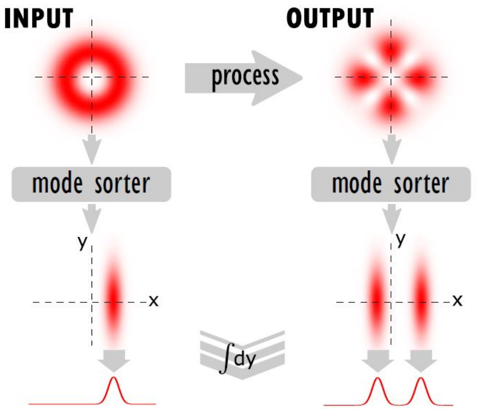

Figura 16 – Sketch of the general process of determining the OAM of a LG beam using a mode sorter. The OAM components get separated along the x-axis and recorded by a CCD camera. The image is integrated along the y-axis.

two LG modes gives rise to two stripes in the right hand panels.

As we can see in Fig. 11, the intensity profiles of adjacent calibration curves have a significant overlap. This means, that just looking at the position of the peaks of each intensity profile is not enough to determine the weighted distribution of OAM components. We overcome this difficulty by fitting the intensity distributions at the output of the mode sorter to the calibration curves. Each intensity profile is determined by the intensity values at each horizontal position after integration over all vertical pixels. So we can write each calibration curve x_i as a vector with length equal to the number of horizontal pixels of the camera:

$$\boldsymbol{x}_i = \{x_k\}_i \ , \tag{4.3}$$

where $-15 \leq i \leq 15$ is an index labeling the input OAM (ℓ), and k labels the CCD camera pixels along the horizontal axis. We can also write the measurement output in terms of vectors:

$$\boldsymbol{y}_j = \{y_k\}_j \ , \tag{4.4}$$

where j labels the measurement of the output OAM and k is the same label as in Eq. (4.3), related to the horizontal position. Every possible measured output can now be expressed as a superposition of the calibrations, i.e.

$$\boldsymbol{y}_j = \sum_{i=-15}^{15} a_i \boldsymbol{x}_i \ , \tag{4.5}$$

where a_i are real and non-negative numbers, corresponding to the weight of each OAM component in the measured output. Now we want to find the values a_i that fit our experimental data the best. To do so we use a linear least squares approach, which means we numerically solve the minimization problem

$$\min_{a_i} \left\| y_j - \sum_{i=-15}^{15} a_i x_i \right\|^2 \ . \tag{4.6}$$

Like this, we can calculate a different vector of OAM weights $\boldsymbol{a}_j = \{a_i\}_j$ for every measurement y_j. To the calculation we have to add the constraint that all elements of $\boldsymbol{a}_j$ are non-negative. This constraint comes from the assumption that the overall phases of each OAM mode component are the same, or that the OAM components are at least far enough from each other so they don't interfere, thus their relative phase is insignificant. Another constraint is that all elements of $\boldsymbol{a_j}$ have to sum to 1. This means the applied process is unitary and therefore has no losses (no optical loss). These assumptions ($a_i \geq 0$, $\sum\limits_i a_i = 1$) can be made without loss of generality.

Instead of solving this problem separately for every recorded image, we can write the process performed by SLM2 as a matrix $\boldsymbol{A}$ and solve one minimization problem for all measurements of the same process at once. This process $\boldsymbol{A}$ then acts on the set of possible input modes $\boldsymbol{X} = \{x_k\}_i$ resulting in the set of measurement outcomes

$\boldsymbol{Y} = \{y_k\}_j$, so

$$\begin{gathered}
\boldsymbol{Y} = \boldsymbol{A}\boldsymbol{X} \\
\begin{pmatrix} \{y_k\}_1 \\ \vdots \\ \{y_k\}_j \end{pmatrix} = \begin{pmatrix} \{a_i\}_1 \\ \vdots \\ \{a_i\}_j \end{pmatrix} \begin{pmatrix} \{x_k\}_1 \\ \vdots \\ \{x_k\}_i \end{pmatrix} \\
\begin{pmatrix} y_{1,1} & y_{1,2} & \dots \\ \vdots & \ddots & \\ y_{j,1} & & y_{j,k} \end{pmatrix} = \begin{pmatrix} a_{11} & a_{12} & \dots \\ \vdots & \ddots & \\ a_{j,1} & & a_{j,i} \end{pmatrix} \begin{pmatrix} x_{1,1} & x_{1,2} & \dots \\ \vdots & \ddots & \\ x_{i,1} & & x_{i,k} \end{pmatrix}
\end{gathered} \tag{4.7}$$

In this way, if we look at Eq. (4.7) as a system of linear equations, each line is equal to Eq. (4.5). Now we can use the linear least squares approach again to numerically solve the minimization problem

$$\min_{\boldsymbol{A}} \ \left\|\boldsymbol{Y} - \boldsymbol{A}\boldsymbol{X}\right\|^2 \ . \tag{4.8}$$

Here, all elements of the matrix $\boldsymbol{A}$ have to be non-negative and all elements in each line of matrix $\boldsymbol{A}$ have to sum to 1. With this approach, if we just consider one measurement of the process for each different ℓ as an input (for example $-7 \leq \ell \leq +7$), the matrix $\boldsymbol{A}$ is equal to the transition probability matrix shown in Fig. 17.

The calculations including the constraints have been done numerically by programs written in the programming languages *Python*, *R* and *Mathematica*.

5 RESULTS

5.1 SIMULATION OF A QUANTUM SYSTEM

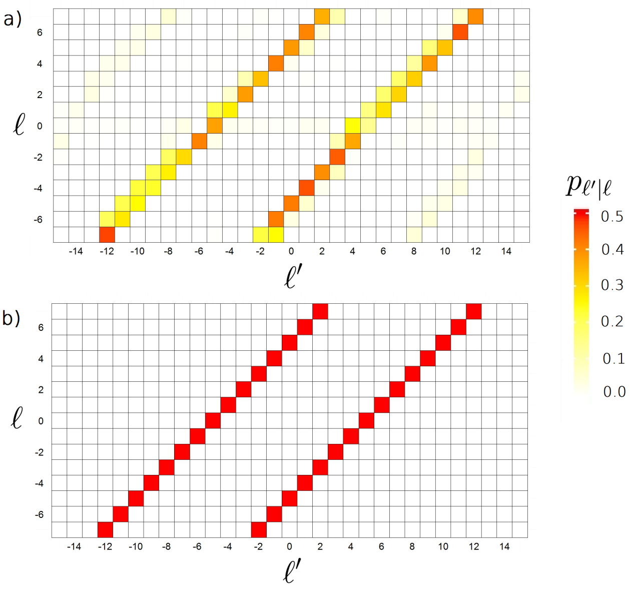

Figura 17 – Conditional probabilities for the process $(\mathcal{L}_{+5} + \mathcal{L}_{-5})/\sqrt{2}$. Input and output are vertical and horizontal axis, respectively. (a) Transition matrix obtained from the recorded experimental data for input modes $-7 \leq \ell \leq 7$. (b) Theoretical prediction for the same process.

With the experimental setup described in chapter 4, we measure the conditional transition probabilities $p_{\ell'|\ell}$ [eq.(3.24)]. To do so we use SLM1 to generate Laguerre-Gaussian modes containing OAM and apply the process $(\mathcal{L}_{+5} + \mathcal{L}_{-5})/\sqrt{2}$ with SLM2. We produce input states ranging from $-7 \leq \ell \leq 7$. This means we are operating in the regime of low temperatures where the Boltzmann weights for $|\ell| > 7$ can be neglected, i.e. $\beta\hbar\omega \gtrapprox 1$, i.e. $\hbar\omega \gtrapprox k_B T$. After we performed the calibration measurements (grey curves in Fig. 11) we recorded 15 measurements, one for each input mode. Two typical results for measurements are shown in Fig. 11 a) and b), where the red curves are the input mode and the green curves are the measured outputs after the process has been applied. Afterwards we solved the minimization problem from Eq. (4.8) for our recorded data. The result for the matrix **A** is the transition probability matrix shown in Fig. 17 a) as a density plot. The plot for an ideal process is shown in Fig. 17 b) for comparison. The labels on the vertical axis are the input modes and the labels on the horizontal axis are the measured output modes. We can see the resulting beams contain OAM of the adjacent modes as well, apart from the expected modes for an ideal process.

With these conditional transition probabilities we can now calculate the work probability distribution $P(W)$ as described in section 3.4. The thermal weights $p(\ell)$ are calculated from Eq. (3.21). The work distribution changes for different β as the probability weights of a thermal state depend on β. A plot of a work distribution for $\beta\hbar\omega = 2$ is shown in Fig. 18. The probability in the vertical axis is obtained summing up all contributions from orbital angular momentum transitions that result in the same work W [Eq. (3.23)], for a given inverse temperature $\beta\hbar\omega$.

Using the results of the work probability distributions we can then evaluate Jarzynski's equality. The average in Eq. (3.38) is taken over the work probability distribution, so that we can explicitly write:

$$\langle e^{-\beta W} \rangle \equiv \int dW \; P(W) \; e^{-\beta W} = e^{-\beta \Delta F} \; . \tag{5.1}$$

For the applied process, the initial Hamiltonian is not changed. Each LG mode corresponds to one energy level and the process couples different LG modes. This is equivalent to transitions between energy levels. Thus, the energy levels do not change but the process induces transitions from one energy level to another (which correspond to the geometry of LG modes family). This means that $\Delta F = 0$ for this process and the right hand side of equation (5.1) equals one.

$$\Rightarrow \langle e^{-\beta W} \rangle = 1 \tag{5.2}$$

The plot of $\langle e^{-\beta W} \rangle$ for different values of $\beta\hbar\omega$ is shown in Fig. 19. For $\beta \lesssim 1$ we obtain $\langle e^{-\beta W} \rangle < 1$. This is due to the fact that we have truncated the range of the input states to $-7 \leq \ell \leq 7$ and for high temperatures or small $\beta\hbar\omega$, this truncation is not valid anymore. This is apparent as the theoretically calculated curve is less than unity for those values as well. The theoretical curve converges to 1 for higher

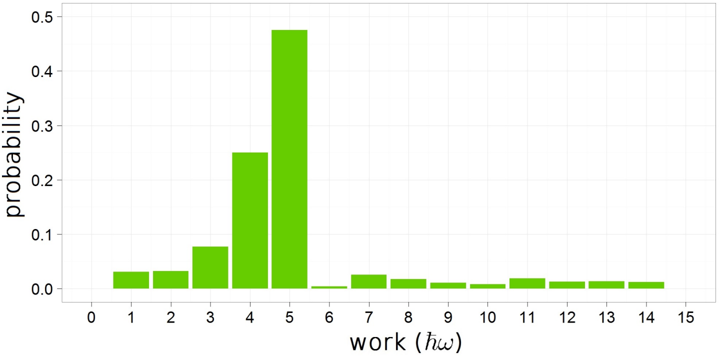

Figura 18 – Experimentally reconstructed work probability distribution for $\beta\hbar\omega = 2$ for the process $(\mathcal{L}_{+5} + \mathcal{L}_{-5})/\sqrt{2}$.

values of $\beta\hbar\omega$. However, the experimental curve always stays below 1 even for lower temperatures ($\beta\hbar\omega > 1$). We interpret this as a consequence of entropy increase due to the action of real world measurement (which includes classical fluctuations coming from laser pointing instability, mechanical vibrations on the set-up and camera thermal noise) and experimental imperfections (such as misalignment, limited pixel resolution on the SLM and on the camera and limited optical resolution on the mode sorter). The width of the experimental curve in Fig. 19 displays the uncertainty, but only accounts for fluctuations. These fluctuations have been detected upon several subsequent identical measurements. For example, for $\beta\hbar\omega = 2$ and in a 95%-confidence interval we have found $e^{-\beta W} = 0.910 \pm 0.046$. The remaining difference to the theory curve is attributed to the experimental imperfections listed above that are not captured by our error estimation procedure, but that is captured by the Jarzynski's fluctuation relation.

5.2 MAXWELL'S DEMON

For the unital process [Eq. (4.1)] we evaluated the Jarzynski relation from equation (5.1). However, in a context that includes measurements and feedback, for example when Maxwell's demon comes into play, the equality no longer holds. In this case the relation in equation (3.52) applies, which includes information as a resource. The demon could extract information from the system with $\sigma \geq -I$ to decrease the

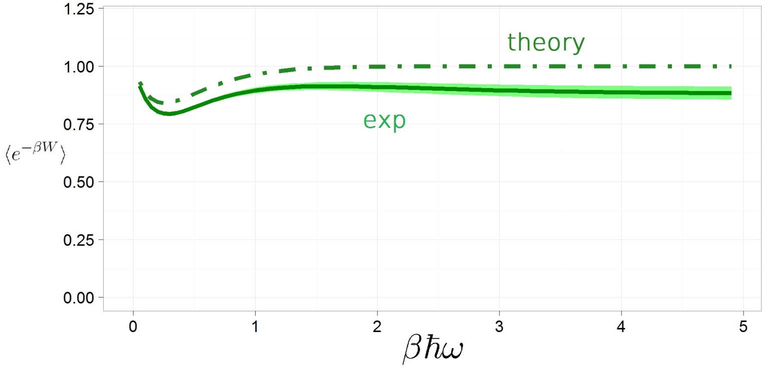

Figura 19 – Plot of the fluctuation relation $\langle e^{-\beta W}\rangle$ for the process $(\mathcal{L}_{+5} + \mathcal{L}_{-5})/\sqrt{2}$. The curve labeled *exp* was obtained from experimental data and the curve labeled *theory* is the theoretically calculated curve for the same process.

entropy production σ.

This section is divided into three parts. First we will present a possible experimental setup that realizes an implementation of a Maxwell's demon to apply conditional operations. This proposal shows a possibility to explore aspects like a feedback control for thermodynamic systems, by using the experimental platform we provide in this work. The second part consists of the evaluation of the Jarzynski's equation including the action of a Maxwell's demon by post-selecting the data we have recorded and was presented in Sec. 5.1. In the third part we show the results of an experimental realization and measurement of a feedback control mechanism. We used the same experimental setup as it was used in the previous section (5.1). In this part we generated a thermal state and applied conditional processes based on extracted information on the generated input states.

5.2.1 Experimental scheme for a Maxwell's Demon

To get insights on such processes that include a Maxwell's Demon, we propose an experimental scheme, using OAM modes. A possible experimental setup of the scheme is shown in figure 20. A laser beam is sent to a spatial light modulator (SLM1), which produces a

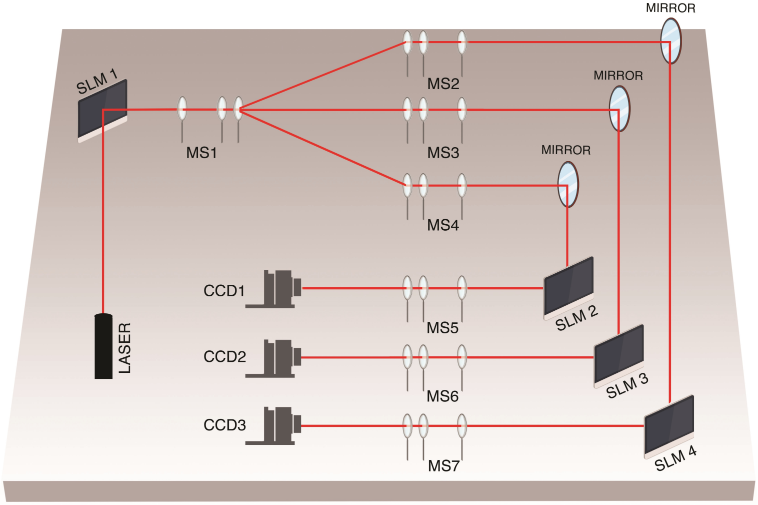

Figura 20 – Experimental setup for a protocol including a Maxwell's demon. After SLM1 generates LG modes from an initial Gaussian laser beam, mode sorter MS1 separarates the modes according to the sign of their OAM (ℓ). Mode sorters MS2, MS3 and MS4 are working in reverse, transforming the light beams into OAM modes, which get spatially modulated by SLM2, SLM3 and SLM4. The OAM of the resulting beams is measured by a mode sorter and a CCD camera (MS5+CCD1, MS6+CCD2 and MS7+CCD3).

thermal state using OAM modes in the same fashion as discussed in chapter 4. The light, prepared in a thermal state, then passes through a mode sorter (MS1), where modes with positive and negative OAM are separated horizontally. Modes with negative OAM are deflected to the left and are sent to mode sorter MS2, modes with $\ell = 0$ do not change their direction and go to mode sorter MS3, while modes with positive OAM are deflected to the right and will pass through mode sorter MS4. The three mode sorters are working in reverse (FICKLER et al., 2014; HUANG et al., 2015). This means the light beam coming from mode sorter MS1 will be converted back into OAM modes. As the input modes are now separated according to their sign of ℓ, we can apply separate operations to them. For modes with positive ℓ we apply the operation $\mathcal{L}_{-5}$ using SLM2, for modes with $\ell = 0$ we apply the operation $(\mathcal{L}_{-5} + \mathcal{L}_{-5})/\sqrt{2}$ using SLM3 and for modes with negative

ℓ we apply the operation $\mathcal{L}_{+5}$ using SLM4. Mode sorters MS5, MS6 and MS7 together with CCD cameras CCD1, CCD2 and CCD3 then perform the final measurement of the OAM in the same way as it has been described in the previous chapter.

This means that the measurement and feedback (or in short the demon) extract information on the sign of ℓ of the input mode, in order to apply conditionally the two operations $\mathcal{L}_{+5}$ and $\mathcal{L}_{-5}$. This results in an increased probability of lowering the absolute value of the OAM ($|\ell|$) of the system, which finally means extracting work from the input thermal state. To illustrate the action of the demon we consider the input mode with an OAM with $\ell = 3$. Without the demon the operation $(\mathcal{L}_{+5} + \mathcal{L}_{-5})/\sqrt{2}$ is applied, which results in $\ell = -2$ or $\ell = +8$ with equal probabilities. This means work of $-\hbar\omega$ or $+5\hbar\omega$ is done on the system, resulting in an average work of $2\hbar\omega$. If the demon takes action the result will always and only be $\ell = -2$, leading to work extracted from the system ($W = -\hbar\omega < 0$).

The measurement of the sign of the OAM means that Maxwell's demon extracts one bit of information (either positive or negative), $I = \ln 2$. For an ideal case this will change the Jarzynski fluctuation relation from equation (3.53) with a demon's action to

$$\langle e^{-\sigma} \rangle = 2 \; . \tag{5.3}$$

5.2.2 Post-selected Process

To evaluate Jarzynski's relation for such a process that includes the action of a Maxwell's demon we want to calculate $\langle e^{-\sigma} \rangle$ again for our measurements of the probability transitions. To do so we post-select the data for the measured conditional probability transitions. We post-select the data in the way that the result is equivalent to the resulting measurement data of the process including a Maxwell's demon that acts exactly in the way described in the experimental proposal of Sec. 5.2.1. The post-selected data for the process including the action of a Maxwell's demon can be seen in Fig. 21 a) next to the probability transitions for the ideal process in Fig. 21 b).

In the same way as before we can calculate the work probability distributions using these results. A work probability distribution for $\beta\hbar\omega = 2$ is shown in Fig. 22. If we compare the work distributions in figures 18 and 22 we note that even though the value of $\langle e^{-\sigma} \rangle$ should change drastically from 1 to 2, the average work hardly chan-

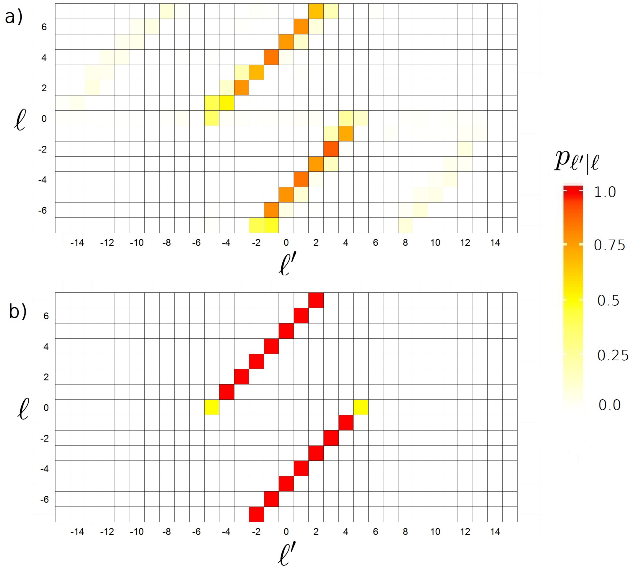

Figura 21 – Conditional probabilities for the process $(\mathcal{L}_{+5} + \mathcal{L}_{-5})/\sqrt{2}$ including the action of a Maxwell's demon. Input and output are vertical and horizontal axis, respectively. (a) Transition matrix obtained from the post-selected recorded experimental data for input modes $-7 \leq \ell \leq 7$. (b) Theoretical prediction for the same process.

ges. Without Maxwell's demon the average work $\langle W \rangle = 5.0\ \hbar\omega$ and with a demon $\langle W \rangle = 4.8\ \hbar\omega$. This is because for low temperatures like $\beta\hbar\omega = 2$ the contribution of the state component with $\ell = 0$ in the input thermal state is rather big (compare with the thermal state in Fig. 12 with a temperature of $\beta\hbar\omega = 0.69$). For an input mode with $\ell = 0$, $\mathcal{L}_{+5}$ and $\mathcal{L}_{-5}$ result in positive work, which dominates the work distribution. We then again evaluate the Jarzynski's relation. A plot is shown in Fig. 23. The curve labeled as *exp* was computed for the post-selected experimental data. The curve labeled *theory* was calculated for an ideal process. The values of $\langle e^{-\sigma} \rangle$ below 2 for high temperatures ($\beta\hbar\omega < 2$) are again due to the truncation of the range of OAM input modes. The uncertainty band of the experimental curve was calculated in the same way as for the experimental curve in Fig. 19. Apart from this uncertainty the additional experimental noise decreases the value of $\langle e^{-\sigma} \rangle$ for any value of $\beta\hbar\omega$. This means that the noise reduces the

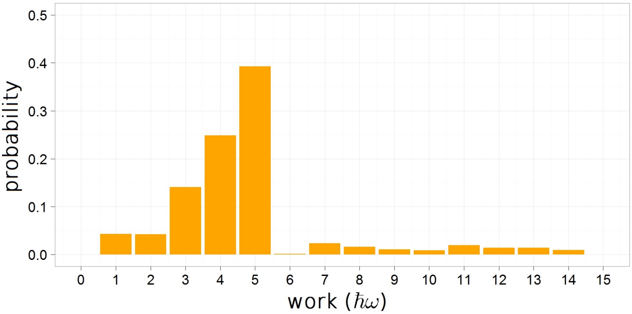

Figura 22 – Experimentally reconstructed work probability distribution for $\beta\hbar\omega = 2$ for the process $(\mathcal{L}_{+5} + \mathcal{L}_{-5})/\sqrt{2}$, including the action of a Maxwell's Demon.

effect caused by the Maxwell's demon, which is to decrease the entropy production of the process.

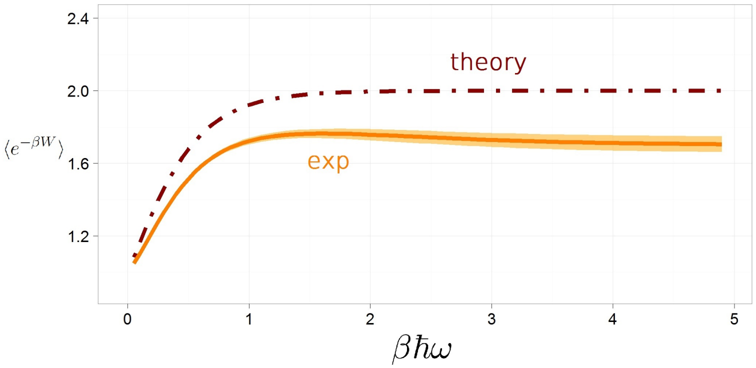

Figura 23 – Plot of the fluctuation relation $\langle e^{-\beta W}\rangle$ for the process $(\mathcal{L}_{+5}+\mathcal{L}_{-5})/\sqrt{2}$ including the action of a Maxwell's demon. The curve labeled *exp* was obtained from experimental data and the curve labeled *theory* is the theoretically calculated curve for the same process.

5.2.3 Experimental implementation of a Maxwell's Demon

We want to further investigate the action of the Maxwell's demon on such a process. For this purpose we implement and measure a feedback control mechanism. To do so we use the same experimental setup as in Fig. 9. In fact there are some minor changes, like the laser used, that do not change the scheme or idea of the experiment (for details on the differences in the experimental setups see Appendix B). This time we implement the operation

$$\mathcal{L}_{+1}\cdot\mathcal{L}_{-1}\cdot\mathcal{L}_{0}\ . \tag{5.4}$$

This means an arbitrary input OAM mode $|\ell\rangle$, results in just one of the modes $|\ell+1\rangle$, $|\ell-1\rangle$ or $|\ell\rangle$, with equal probability. Instead of applying one of the three possible actions $(\mathcal{L}_{+1},\mathcal{L}_{-1},\mathcal{L}_{0})$ with probability 1/3 for each, we want the feedback control and the Maxwell's demon to act in the following way: Extract the information of the sign of ℓ of the input OAM mode generated by SLM1 and then use this information to apply a conditional process with SLM2 that decreases the entropy production rate. For input modes with negative ℓ we want to apply the operation $\mathcal{L}_{+1}$, for positive ℓ the operation $\mathcal{L}_{-1}$ and for $\ell=0$ the identity operation $\mathcal{L}_{0}$.

This implementation is equivalent to the experimental proposal in Sec. 5.2.1 if we adjust the operations performed by SLM2, SLM3 and SLM4 in Fig. 20 accordingly.

In section 5.1 we measured the conditional probability transitions and then calculated the work probability distributions using the theoretical weights for the thermal input states for different values of β. In this experiment we want to emulate a thermal state. To do so the input modes are randomly chosen by a computer according to the thermal probability distribution defined by Eq. 3.21 and are then generated by SLM1. We generate one Laguerre-Gaussian beam with ℓ at a time and for 3 seconds each. We produce 400 separate input modes for a fixed value of $\beta\hbar\omega$ (the probability weights for each input state depend on β). Like this, 400 performed measurements for the same applied process are approximately equivalent to a single measurement of the process applied to a single thermal state with $\beta\hbar\omega$. This way of simulating a thermal state is valid due to the fact that a thermal state is a mixed state [Eq. (3.16)]. In quantum mechanics a mixed state is a sum of pure states, which here are the separately generated input modes. We can then incoherently add those input modes to obtain a mixed state equivalent to a thermal state. Furthermore, performing the measurement on the different OAM components on a final output state is equivalent to taking the partial trace of our quantum system for each separate subspace, which is equivalent to performing separate projective measurements. With the same argument we justify the fact that by always just applying one of the operations $\mathcal{L}_{+1}$, $\mathcal{L}_{-1}$ or $\mathcal{L}_0$ we implement the process (5.4).

Even though the input modes are selected randomly, the information about which mode is being generated is accessible in the computer that picked the modes in the first place. In our experiment the demon extracts the information about the sign of each input mode. Extracting this information is equivalent to a projective feedback measurement. This information then is used to decide which operation will be applied by SLM2. This implementation of a Maxwell's demon is equivalent to that presented in Sec. 5.2.1.

The implementation of Maxwell's demon in this fashion has the advantage that the success of extracting information (probability of a successful feedback measurement) can be controlled through a parameter $\mathcal{I} \in [0, 1]$. For example for $\mathcal{I} = 0.5$ the demon is just able to extract the information about the input mode with a probability of 0.5 .

A brief summary of one measurement cycle would be:
A computer chooses a random value ℓ according to a thermal distri-

bution for a fixed value of β; SLM1 generates a LG mode with ℓ for 3 seconds; with the probability $\mathcal{I}$ the computer uses the information on the sign of ℓ to apply an operation with SLM2 according to the Maxwell's demon protocol (if the information is not extracted, one of the operations $\mathcal{L}_{+1}$, $\mathcal{L}_{-1}$ or $\mathcal{L}_0$ is chosen randomly with probability 1/3); a projective measurement is performed using the mode sorter and a CCD camera; these steps are repeated 400 times.

One cycle like this corresponds to one measurement for a process on one thermal state for a fixed value of β and $\mathcal{I}$. One measurement cycle will result in a single data point in Figs. 24 and 25.

We compute the minimization problem from Eq. 4.6 for every recorded image to obtain the transition probabilities. With this data we can extract directly the information for the work probability distribution for the emulated thermal state. Finally we can use these results to evaluate Jarzynksi's relation. The results of the experiment are shown in Fig. 24. Each data point of the curve labeled *exp* corresponds to the computations of $\langle e^{-\beta W}\rangle$ from the measured data of one measurement cycle for a fixed value of $\beta\hbar\omega$ and $\mathcal{I} = 1$. The result for an ideal process is shown in the curve labeled *theory.* As the demon extracts the information of the OAM (ℓ) being either positive, negative or equal to zero, the extracted information is $I = \ln(3\mathcal{I})$. So including the action of the demon, Jarzynski's relation reads

$$\begin{aligned} & \langle e^{-\sigma-I}\rangle = 1 \\ \Leftrightarrow\quad & \langle e^{-\sigma} e^{-\ln 3\mathcal{I}}\rangle = 1 \\ \Leftrightarrow\quad & \langle e^{-\sigma}\frac{1}{3\mathcal{I}}\rangle = 1 \\ \Leftrightarrow\quad & \langle e^{-\sigma}\rangle = 3\mathcal{I}\ . \end{aligned} \tag{5.5}$$

For an ideal feedback control mechanism we get $\langle e^{-\sigma}\rangle = 3$. The theoretical curve just converges to 3 for low enough temperatures ($\beta\hbar\omega > 3$) as a consequence of the truncation of the input thermal state. The *exp* curve always stays below the theoretical curve. This is due to the same experimental imperfections and uncertainties as mentioned as in Sec. 5.1. Another reason for the difference between the curves is the fact that the thermal state was emulated by 400 random values of ℓ. As $\beta\hbar\omega$ increases, the weights of larger ℓ decrease and this leads to a more inaccurate approximation of a thermal state by just 400 random values. As the contribution to $\langle e^{-\beta W}\rangle$ is exponential in $\beta\hbar\omega$, the difference between the results for an emulated thermal state and a theoretically calculated thermal state gets bigger. To make this visible we

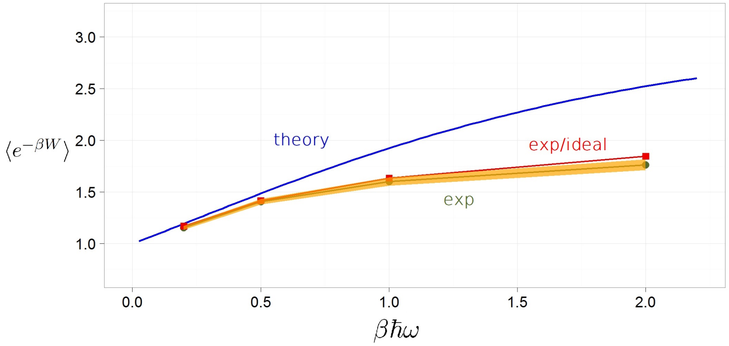

Figura 24 – Plot of the fluctuation relation $\langle e^{-\beta W}\rangle$ for the process $(\mathcal{L}_{+1} + \mathcal{L}_{-1} + \mathcal{L}_0)/\sqrt{3}$. The curve labeled *exp* was calculated from experimental data, the curve labeled *exp/ideal* was calculated for the random input states, but for a theoretically computed ideal process and the curve labeled *theory* was calculated for a theoretical thermal state for an ideal process.

plotted the curve labeled *exp/ideal*. This curve was calculated for the thermal states that were emulated by the 400 random values, but an ideal process was applied to exclude measurement noise.

In order to get further insight on the process of a feedback measurement we varied the parameter $\mathcal{I}$. The result is shown in Fig. 25. The values of $\langle e^{-\sigma}\rangle$ are again lower than the expected value of 3 due to truncation of the input modes, uncertainty and experimental imperfections. The values of $\langle e^{-\sigma}\rangle$ increase with $\mathcal{I}$ as predicted by equation (5.5). The approximate linear relation is plotted in Fig. 25 b). By varying the parameter $\mathcal{I}$ we can simulate noise in the feedback measurement process of Maxwell's demon.

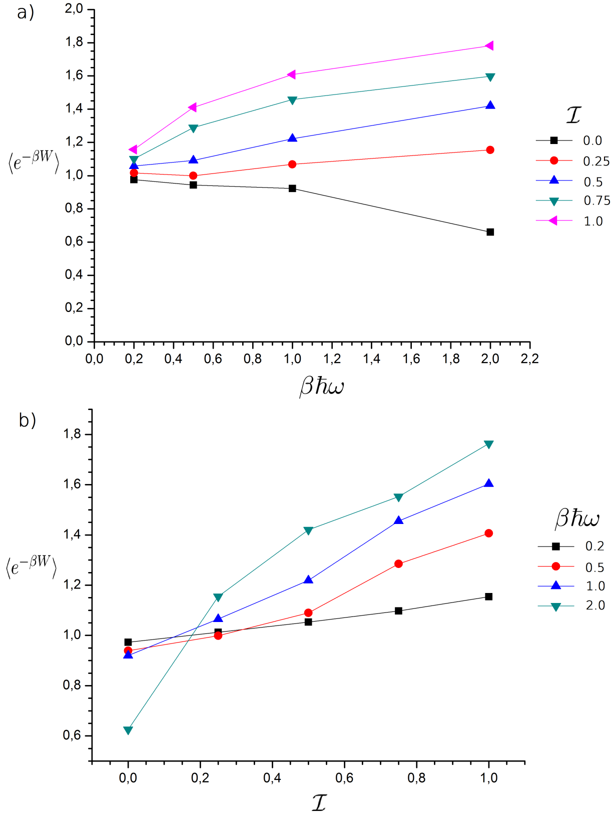

Figura 25 – Plot of the fluctuation relation $\langle e^{-\beta W}\rangle$ for the process $(\mathcal{L}_{+1} + \mathcal{L}_{-1} + \mathcal{L}_0)/\sqrt{3}$. The plot in a) is showing the relation between $\langle e^{-\beta W}\rangle$ and $\beta\hbar\omega$ for different fixed values of $\mathcal{I}$, and plot b) is showing the relation between $\langle e^{-\beta W}\rangle$ and $\mathcal{I}$ for different fixed values of $\beta\hbar\omega$.

6 CONCLUSIONS

In this work we have exploited the analogy between the paraxial wave equation and the Schrödinger equation to simulate experimentally a quantum system using the orbital angular momentum of light. The orbital angular momentum of a light beam is a discrete degree of freedom with infinite dimension that we used by creating and manipulating Laguerre-Gaussian beams through spatial modulation of those light beams. It is usually employed in applications of quantum communication and quantum information processing in the single-photon regime to realize a qudit. Here we simulated the energy eigenstates of a quantum harmonical oscillator and their evolution through a given process and used those energy eigenstates to generate optical thermal states. With the experimental setup we presented, it is possible to investigate the quantum version of the thermodynamic work and Jarzynski's fluctuation relation of a quantum system. To do so we measured the work distribution of a given process and were able to obtain the experimental Jarzynski's fluctuation relation. Further we proposed an experimental scheme that separates input modes according to the sign of the orbital angular momentum of a light beam (sign of ℓ) into different paths to apply different conditional operations and therefore implements a Maxwell's demon. A Maxwell's demon has been implemented experimentally by using the extracted information about the sign of ℓ to control a feedback action. In this experiment a thermal state was simulated by the random generation of input modes according to the thermal probability weights. The advantage of a simulation of a thermal state in this fashion is that the probability of a successful feedback measurement can be controlled. With the experimental platform presented in this work, we can simulate and manipulate a quantum system and perform projective measurements of the energy eigenstates. We are able to apply operations to the simulated system corresponding to the evolution of the system and therefore study its thermodynamical aspects. Furthermore we can implement and control a measurement feedback control mechanism.

These results show the usefulness of employing the orbital angular momentum of Laguerre-Gaussian beams as a computational basis in order to investigate aspects of the growing field of quantum thermodynamics in high dimensional Hilbert spaces. Given the versatility of this platform, one can consider using it, for example, in the study of the role of multipartite entanglement in thermodynamic processes, as well as the role of the environment, i.e., non-unitary and non-unital processes.

REFERÊNCIAS

ALLEN, L. et al. Orbital angular momentum of light and the transformation of laguerre-gaussian laser modes. **Phys. Rev. A**, American Physical Society, v. 45, p. 8185–8189, Jun 1992. Disponível em: <https://link.aps.org/doi/10.1103/PhysRevA.45.8185>.

ALMEIDA, J. O. de. **Manipulação de feixes com momento angular orbital**. Dissertação (Mestrado) — Universidade Federal do Rio de Janeiro, 2015.

AO, T. B. B. et al. Experimental reconstruction of work distribution and study of fluctuation relations in a closed quantum system. **Phys. Rev. Lett.**, American Physical Society, v. 113, p. 140601, Oct 2014. Disponível em: <https://link.aps.org/doi/10.1103/PhysRevLett.113.140601>.

ARAúJO, R. M. de et al. Experimental study of quantum thermodynamics using optical vortices. **Journal of Physics Communications**, v. 2, n. 3, p. 035012, 2018. Disponível em: <http://stacks.iop.org/2399-6528/2/i=3/a=035012>.

BERKHOUT, G. C. G. et al. Efficient sorting of orbital angular momentum states of light. **Phys. Rev. Lett.**, American Physical Society, v. 105, p. 153601, Oct 2010. Disponível em: <https://link.aps.org/doi/10.1103/PhysRevLett.105.153601>.

BOCHKOV, G.; KUZOVLEV, Y. Nonlinear fluctuation-dissipation relations and stochastic models in nonequilibrium thermodynamics: I. generalized fluctuation-dissipation theorem. **Physica A: Statistical Mechanics and its Applications**, v. 106, n. 3, p. 443 – 479, 1981. ISSN 0378-4371. Disponível em: <http://www.sciencedirect.com/science/article/pii/0378437181901229>.

Bochkov, G. N.; Kuzovlev, Y. E. General theory of thermal fluctuations in nonlinear systems. **Soviet Journal of Experimental and Theoretical Physics**, v. 45, p. 238–247, jan. 1977.

BOSE, S. N.; EISNTEIN, A. Plancks gesetz und lichtquantenhypothese. **Zeitschrift für Physik**, v. 26, 1924.

BOURENNANE, M.; KARLSSON, A.; BJÖRK, G. Quantum key distribution using multilevel encoding. **Phys. Rev. A**, American

Physical Society, v. 64, p. 012306, Jun 2001. Disponível em: <https://link.aps.org/doi/10.1103/PhysRevA.64.012306>.

CALLEN, H. B.; WELTON, T. A. Irreversibility and generalized noise. **Phys. Rev.**, American Physical Society, v. 83, p. 34–40, Jul 1951. Disponível em: <https://link.aps.org/doi/10.1103/PhysRev.83.34>.

CAMATI, P. A. et al. Experimental rectification of entropy production by maxwell's demon in a quantum system. **Phys. Rev. Lett.**, American Physical Society, v. 117, p. 240502, Dec 2016. Disponível em: <https://link.aps.org/doi/10.1103/PhysRevLett.117.240502>.

CAMPISI, M. et al. Employing circuit qed to measure non-equilibrium work fluctuations. **New Journal of Physics**, v. 15, n. 10, p. 105028, 2013. Disponível em: <http://stacks.iop.org/1367-2630/15/i=10/a=105028>.

CAMPISI, M.; HÄNGGI, P.; TALKNER, P. Colloquium: Quantum fluctuation relations: Foundations and applications. **Rev. Mod. Phys.**, American Physical Society, v. 83, p. 771–791, Jul 2011. Disponível em: <https://link.aps.org/doi/10.1103/RevModPhys.83.771>.

CAMPISI, M.; TALKNER, P.; HÄNGGI, P. Quantum bochkov–kuzovlev work fluctuation theorems. **Philosophical Transactions of the Royal Society of London A: Mathematical, Physical and Engineering Sciences**, The Royal Society, v. 369, n. 1935, p. 291–306, 2011. ISSN 1364-503X. Disponível em: <http://rsta.royalsocietypublishing.org/content/369/1935/291>.

COMMONS, W. **helical beam with different topological charge.** 2011. Disponível em: <https://commons.wikimedia.org/wiki/File:Helixoam.png>.

CROOKS, G. E. Nonequilibrium measurements of free energy differences for microscopically reversible markovian systems. **Journal of Statistical Physics**, v. 90, n. 5, p. 1481–1487, Mar 1998. ISSN 1572-9613. Disponível em: <https://doi.org/10.1023/A:1023208217925>.

CROOKS, G. E. Entropy production fluctuation theorem and the nonequilibrium work relation for free energy differences. **Phys. Rev.**

E, American Physical Society, v. 60, p. 2721–2726, Sep 1999. Disponível em: <https://link.aps.org/doi/10.1103/PhysRevE.60.2721>.

DADA, A. C. et al. Experimental high-dimensional two-photon entanglement and violations of generalized bell inequalities. **Nature Physics**, Nature Publishing Group SN -, v. 7, p. 677 EP –, May 2011. Disponível em: <http://dx.doi.org/10.1038/nphys1996>.

DAVIS, J. A. et al. Encoding amplitude information onto phase-only filters. **Appl. Opt.**, OSA, v. 38, n. 23, p. 5004–5013, Aug 1999. Disponível em: <http://ao.osa.org/abstract.cfm?URI=ao-38-23-5004>.

DORNER, R. et al. Extracting quantum work statistics and fluctuation theorems by single-qubit interferometry. **Phys. Rev. Lett.**, American Physical Society, v. 110, p. 230601, Jun 2013. Disponível em: <https://link.aps.org/doi/10.1103/PhysRevLett.110.230601>.

EINSTEIN, A. **Investigations on the Theory of the Brownian Movement**. Dover Publications, 1926. (Dover Books on Physics Series). ISBN 9780486603049. Disponível em: <http://store.doverpublications.com/0486603040.html>.

ESPOSITO, M.; HARBOLA, U.; MUKAMEL, S. Nonequilibrium fluctuations, fluctuation theorems, and counting statistics in quantum systems. **Rev. Mod. Phys.**, American Physical Society, v. 81, p. 1665–1702, Dec 2009. Disponível em: <https://link.aps.org/doi/10.1103/RevModPhys.81.1665>.

FICKLER, R. et al. Interface between path and orbital angular momentum entanglement for high-dimensional photonic quantum information. **Nature Communications**, Nature Publishing Group, a division of Macmillan Publishers Limited. All Rights Reserved. SN -, v. 5, p. 4502 EP –, Jul 2014. Article. Disponível em: <http://dx.doi.org/10.1038/ncomms5502>.

FOWLES, G. **Introduction to Modern Optics**. Dover Publications, 1975. (Dover Books on Physics Series). ISBN 9780486659572. Disponível em: <https://books.google.de/books?id=SL1n9TuJ5YMC>.

GIOVANNINI, D. et al. Characterization of high-dimensional entangled systems via mutually unbiased measurements. **Phys. Rev. Lett.**, American Physical Society, v. 110, p. 143601, Apr 2013. Disponível em: <https://link.aps.org/doi/10.1103/PhysRevLett.110.143601>.

GLOGE, D.; MARCUSE, D. Formal quantum theory of light rays. **J. Opt. Soc. Am.**, OSA, v. 59, n. 12, p. 1629–1631, Dec 1969. Disponível em: <http://www.osapublishing.org/abstract.cfm?URI=josa-59-12-1629>.

HÄNGGI, P.; MARCHESONI, F. Artificial brownian motors: Controlling transport on the nanoscale. **Rev. Mod. Phys.**, American Physical Society, v. 81, p. 387–442, Mar 2009. Disponível em: <https://link.aps.org/doi/10.1103/RevModPhys.81.387>.

HEYL, M.; KEHREIN, S. Crooks relation in optical spectra: Universality in work distributions for weak local quenches. **Phys. Rev. Lett.**, American Physical Society, v. 108, p. 190601, May 2012. Disponível em: <https://link.aps.org/doi/10.1103/PhysRevLett.108.190601>.

HOROWITZ, J.; JARZYNSKI, C. Comparison of work fluctuation relations. **Journal of Statistical Mechanics: Theory and Experiment**, v. 2007, n. 11, p. P11002, 2007. Disponível em: <http://stacks.iop.org/1742-5468/2007/i=11/a=P11002>.

HUANG, H. et al. Mode division multiplexing using an orbital angular momentum mode sorter and mimo-dsp over a graded-index few-mode optical fibre. **Scientific Reports**, The Author(s) SN -, v. 5, p. 14931 EP –, Oct 2015. Article. Disponível em: <http://dx.doi.org/10.1038/srep14931>.

HUBER, G. et al. Employing trapped cold ions to verify the quantum jarzynski equality. **Phys. Rev. Lett.**, American Physical Society, v. 101, p. 070403, Aug 2008. Disponível em: <https://link.aps.org/doi/10.1103/PhysRevLett.101.070403>.

HUBER, M.; PAWŁOWSKI, M. Weak randomness in device-independent quantum key distribution and the advantage of using high-dimensional entanglement. **Phys. Rev. A**, American Physical Society, v. 88, p. 032309, Sep 2013. Disponível em: <https://link.aps.org/doi/10.1103/PhysRevA.88.032309>.

JARZYNSKI, C. Nonequilibrium equality for free energy differences. **Phys. Rev. Lett.**, American Physical Society, v. 78, p. 2690–2693, Apr 1997. Disponível em: <https://link.aps.org/doi/10.1103/PhysRevLett.78.2690>.

JOHNSON, J. B. Thermal agitation of electricity in conductors. **Phys. Rev.**, American Physical Society, v. 32, p. 97–109, Jul 1928. Disponível em: <https://link.aps.org/doi/10.1103/PhysRev.32.97>.

KRAUS, A. B. K. **States Effects and Operations: Fundamental Notions of Quantum Theory (Lecture Notes in Physics)**. [S.l.]: Springer-Verlag Berlin Heidelberg, 1983.

KRENN, M. et al. Generation and confirmation of a (100 × 100)-dimensional entangled quantum system. **Proceedings of the National Academy of Sciences**, National Academy of Sciences, v. 111, n. 17, p. 6243–6247, 2014. ISSN 0027-8424. Disponível em: <http://www.pnas.org/content/111/17/6243>.

LEMOS, G. B. et al. Experimental observation of quantum chaos in a beam of light. **Nature Communications**, Nature Publishing Group, v. 3, p. 1211, Nov 2012. Disponível em: <https://www.nature.com/articles/ncomms2214>.

MAZZOLA, L.; CHIARA, G. D.; PATERNOSTRO, M. Measuring the characteristic function of the work distribution. **Phys. Rev. Lett.**, American Physical Society, v. 110, p. 230602, Jun 2013. Disponível em: <https://link.aps.org/doi/10.1103/PhysRevLett.110.230602>.

MOLINA-TERRIZA, G.; TORRES, J. P.; TORNER, L. Management of the angular momentum of light: Preparation of photons in multidimensional vector states of angular momentum. **Phys. Rev. Lett.**, American Physical Society, v. 88, p. 013601, Dec 2001. Disponível em: <https://link.aps.org/doi/10.1103/PhysRevLett.88.013601>.

NIELSEN, M. A.; CHUANG, I. L. **Quantum Computation and Quantum Information: 10th Anniversary Edition**. 10th. ed. New York, NY, USA: Cambridge University Press, 2011. ISBN 1107002176, 9781107002173.

NIENHUIS, G.; ALLEN, L. Paraxial wave optics and harmonic oscillators. **Phys. Rev. A**, American Physical Society, v. 48, p. 656–665, Jul 1993. Disponível em: <https://link.aps.org/doi/10.1103/PhysRevA.48.656>.

PADGETT, M. Light's twist. **Proceedings of the Royal Society of London A: Mathematical, Physical and Engineering Sciences**, The Royal Society, v. 470, n. 2172, 2014. ISSN 1364-5021. Disponível em: <http://rspa.royalsocietypublishing.org/content/470/2172/20140633>.

PADGETT, M.; ALLEN, L. Light with a twist in its tail. **Contemporary Physics**, Taylor and Francis, v. 41, n. 5, p. 275–285, 2000. Disponível em: <https://doi.org/10.1080/001075100750012777>.

PEKOLA, J. P. et al. Calorimetric measurement of work in a quantum system. **New Journal of Physics**, v. 15, n. 11, p. 115006, 2013. Disponível em: <http://stacks.iop.org/1367-2630/15/i=11/a=115006>.

PLANCK, M. Zur theorie der wärmestrahlung. **Annalen der Physik**, v. 4, 1910.

POYNTING, J. H. The wave motion of a revolving shaft, and a suggestion as to the angular momentum in a beam of circularly polarised light. **Proceedings of the Royal Society of London A: Mathematical, Physical and Engineering Sciences**, The Royal Society, v. 82, n. 557, p. 560–567, 1909. ISSN 0950-1207. Disponível em: <http://rspa.royalsocietypublishing.org/content/82/557/560>.

RASTEGIN, A. E. Non-equilibrium equalities with unital quantum channels. **Journal of Statistical Mechanics: Theory and Experiment**, v. 2013, n. 06, p. P06016, 2013. Disponível em: <http://stacks.iop.org/1742-5468/2013/i=06/a=P06016>.

RASTEGIN, A. E.; ZYCZKOWSKI, K. Jarzynski equality for quantum stochastic maps. **Phys. Rev. E**, American Physical Society, v. 89, p. 012127, Jan 2014. Disponível em: <https://link.aps.org/doi/10.1103/PhysRevE.89.012127>.

RITORT, F. The nonequilibrium thermodynamics of small systems. **Comptes Rendus Physique**, v. 8, n. 5, p. 528 – 539, 2007. ISSN 1631-0705. Work, dissipation, and fluctuations in nonequilibrium physics. Disponível em: <http://www.sciencedirect.com/science/article/pii/S1631070507000813>.

SAGAWA, T.; UEDA, M. Generalized jarzynski equality under nonequilibrium feedback control. **Phys. Rev. Lett.**, American

Physical Society, v. 104, p. 090602, Mar 2010. Disponível em: <https://link.aps.org/doi/10.1103/PhysRevLett.104.090602>.

SALEH, B. E. A.; TEICH, M. C. **Fundamentals of Photonics**. John Wiley and Sons, Inc., 2001. ISBN 9780471213741. Disponível em: <http://dx.doi.org/10.1002/0471213748.ch3>.

STOLER, D. Operator methods in physical optics. **J. Opt. Soc. Am.**, OSA, v. 71, n. 3, p. 334–341, Mar 1981. Disponível em: <http://www.osapublishing.org/abstract.cfm?URI=josa-71-3-334>.

SVELTO, O. **Principles of Lasers**. Springer US, 1976. ISBN 978-1-4419-1302-9. Disponível em: <https://link.springer.com/book/10.1007

TALKNER, P.; LUTZ, E.; HÄNGGI, P. Fluctuation theorems: Work is not an observable. **Phys. Rev. E**, American Physical Society, v. 75, p. 050102, May 2007. Disponível em: <https://link.aps.org/doi/10.1103/PhysRevE.75.050102>.

Tasaki, H. Jarzynski relations for quantum systems and some applications. **eprint arXiv:cond-mat/0009244**, sep 2000.

VAZIRI, A.; WEIHS, G.; ZEILINGER, A. Experimental two-photon, three-dimensional entanglement for quantum communication. **Phys. Rev. Lett.**, American Physical Society, v. 89, p. 240401, Nov 2002. Disponível em: <https://link.aps.org/doi/10.1103/PhysRevLett.89.240401>.

WALLS, G. M. D. **Quantum Optics**. Springer-Verlag Berlin Heidelberg, 1994. ISBN 978-3-642-79504-6. Disponível em: <http://www.springer.com/gp/book/9783540588313>.

YAO, A. M.; PADGETT, M. J. Orbital angular momentum: origins, behavior and applications. **Adv. Opt. Photon.**, OSA, v. 3, n. 2, p. 161–204, Jun 2011. Disponível em: <http://aop.osa.org/abstract.cfm?URI=aop-3-2-161>.

APÊNDICE A – Measurement uncertainty

In our experiment we determine the orbital angular momentum components of a light beam. We do so by recording a picture and integrating it to obtain its marginal intensity distribution $\boldsymbol{y_j} = \{\boldsymbol{y_{j,k}}\}_{\boldsymbol{k}}$. We want to determine the uncertainty on each $\boldsymbol{y_{i,k}}$ in order to be able to calculate the uncertainty of our results.
To do so a series of ten identical measurements on the same transformed mode over a time window of a few minutes was recorded. Like this, a set of intensity distributions fluctuating for each $\boldsymbol{k}$, around a mean value $\boldsymbol{\mu_k}$ with a standard deviation $\boldsymbol{\sigma_k}$ was obtained. $\boldsymbol{\sigma_{i,k}}$ is the uncertainty on each $\boldsymbol{y_{i,k}}$. These standard deviations depend mostly on $\boldsymbol{\mu_k}$, but as well on $\boldsymbol{k}$ itself. These measurements were used to model the typical error associated to a $\boldsymbol{y_i}$ measurement and we noticed the relative standard deviation $(\boldsymbol{\sigma/\mu})$ is always smaller than 10%, for any $\boldsymbol{k}$. This procedure led to a set of numbers $\boldsymbol{\sigma_{i,k}}$ used as input for our model, in which we assume each $\boldsymbol{y_i}$ measured is a realization of a random variable following the multivariate normal distribution with estimated mean values $\boldsymbol{y_{i,k}}$ and standard deviations $\boldsymbol{\sigma_{i,k}}$. This procedure above allows us to simulate sets of measurements, realizing *Monte Carlo experiments.*
Ten different experimental matrices $\boldsymbol{Y}$ were randomly generated in this manner, from each of which we numerically solved the minimization problem from equation (4.8) with our calibration curves $\boldsymbol{X}$ in order to find a different probability matrix $\boldsymbol{A}$. We could see from the set of matrices $\boldsymbol{A}$ that the relative uncertainty on each matrix element was never bigger than 2%. Similarly (and finally), we performed 1000 Monte Carlo experiments in order to estimate the uncertainty on $\langle \boldsymbol{e^{-\beta W}} \rangle$ for each $\boldsymbol{\beta\hbar\omega}$ ranging from 0.05 to 5. We observed that the random variable $\boldsymbol{e^{-\beta W}}$ nearly follows a normal distribution for all values of $\boldsymbol{\beta\hbar\omega}$. For instance, for $\boldsymbol{\beta\hbar\omega} = 2$ for the process $\boldsymbol{(\mathcal{L}_{+5} + \mathcal{L}_{-5})/2}$, we have found $\langle \boldsymbol{e^{-\beta W}} \rangle = \mathbf{0.910}$ with a standard deviation $\boldsymbol{\sigma} = \mathbf{0.022}$. From the $\mathbf{1.96}\boldsymbol{\sigma}$ rule, we established our 95%-confidence interval for $\boldsymbol{e^{-2W/\hbar\omega}}$ to be $\mathbf{0.910 \pm 0.046}$. By doing the same for all values of $\boldsymbol{\beta\hbar\omega}$, we were able to plot the uncertainty band shown in Fig. 19.

APÊNDICE B – Differences in experimental setup

For the experimental implementation of a Maxwell's demon, explained in Sec. 5.2.3, slightly different elements in the experimental setup were used, compared to the setup described in Sec. 4.1. These changes do not affect the scheme or experimental idea of the experiment and are equivalent in their nature.
In this setup instead of a Ne-He laser, a single mode Diode laser with a wavelength of $\boldsymbol{638\ nm}$ was used. To expand the beam, two lenses with the focal lengths $\boldsymbol{f_1 = 15\ mm}$ and $\boldsymbol{f_2 = 30\ mm}$ were employed to result in a magnification of 2. As the shape of the intensity profile was not approximately a Gaussian shape, we used an iris to filter the beam profile spatially.
Instead of two SLMs, just one SLM was used in the experiment. The SLM display was divided into two halfs, so that the left half was used as SLM1 and the right half of the screen was used as SLM2 in Fig. 9. This means that SLM1/SLM2 were used with 960x1080 pixels instead of 1920x1080 pixels. The beam path of this realization is shown in Fig. 26. The mode sorter and the CCD camera are the same as in section 4.1.

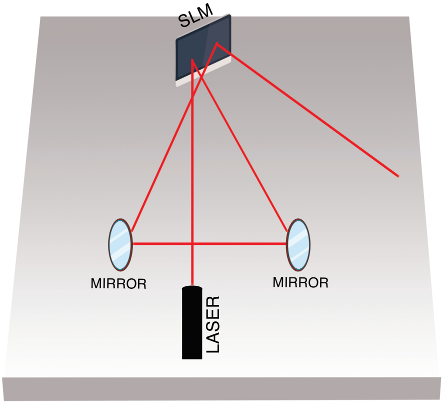

Figura 26 – Beam path to use one SLM for two separate spatial modulations by dividing the screen into half.